iScience

CellPress
OPEN ACCESS

Article

Off-Peak 594-nm Light Surpasses On-Peak 532-nm Light in Silencing Distant ArchT-Expressing Neurons In Vivo

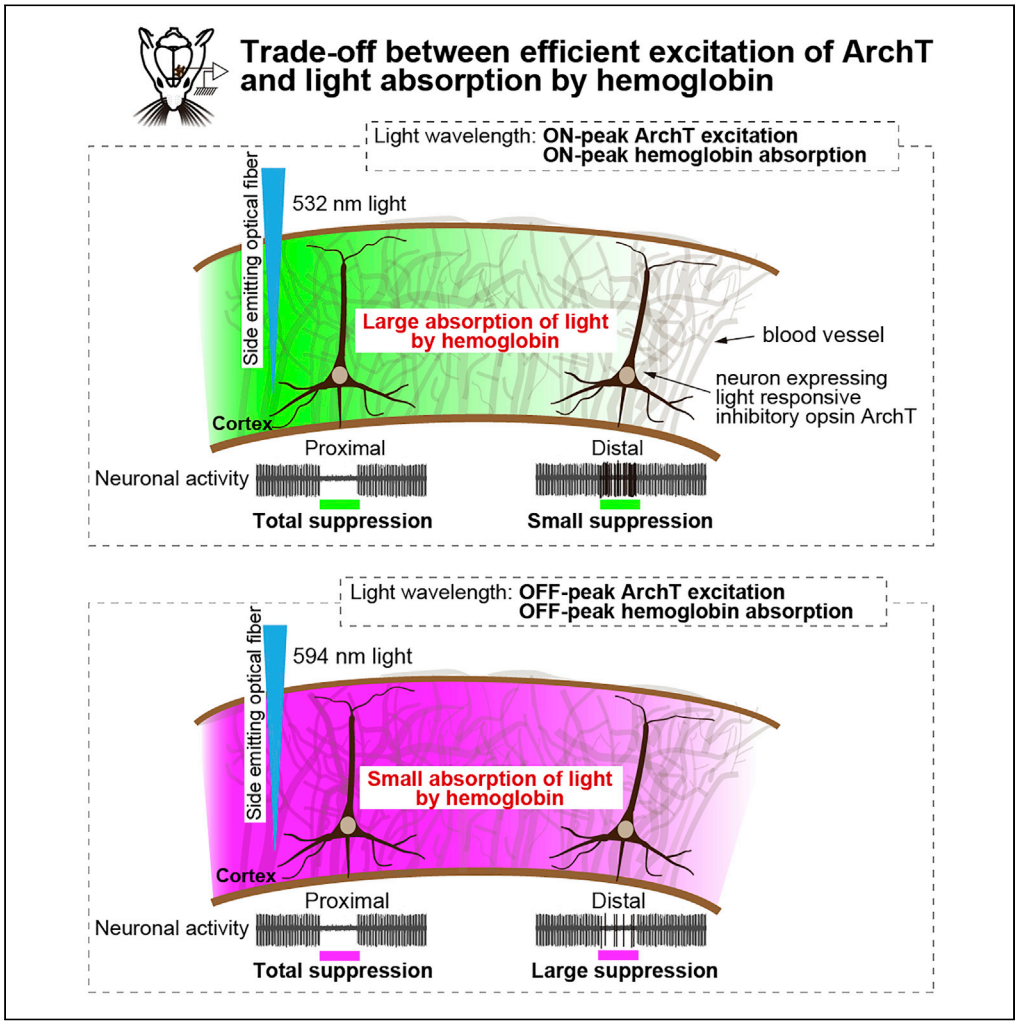

Rieko Setsuie, Keita Tamura, Kentaro Miyamoto, Takamitsu Watanabe, Masaki Takeda, Yasushi Miyashita

rieko.setsuie@riken.jp

HIGHLIGHTS

Wavelength-dependency of optogenetic neuronal control was directly measured *in vivo*

Off-peak light silence 1-mm-distant ArchT-neuron twice more than on-peak light *in vivo*

Superiority of off-peak light at distance arose from its less absorption of light

Simulation of light propagation supported unexpectedly large effect of hemoglobin

Setsuie et al., iScience *23*, 101276
July 24, 2020
https://doi.org/10.1016/j.isci.2020.101276

iScience

CellPress
OPEN ACCESS

Article

Off-Peak 594-nm Light Surpasses On-Peak 532-nm Light in Silencing Distant ArchT-Expressing Neurons In Vivo

Rieko Setsuie,[1,2,3,4,*] Keita Tamura,[1] Kentaro Miyamoto,[1] Takamitsu Watanabe,[3] Masaki Takeda,[1,2] and Yasushi Miyashita[1,2,3]

SUMMARY

For large brain volume manipulations using optogenetics, both effective opsin excitation and efficient light delivery with minimal light absorption are required to minimize the illuminating light intensity and concomitant off-target effects. ArchT, a widely used potent inhibitory opsin, is commonly activated by 532-nm light, which lies on its *in vitro* excitation peak. However, 532-nm light also lies on a peak range of the hemoglobin absorption spectrum. Therefore, we predicted that 594-nm light is superior in suppressing distant ArchT-expressing neurons, which is slightly off the ArchT-excitation-plateau and largely off the peak of the hemoglobin absorption spectrum. We quantitatively tested this prediction by the electrophysiological recording of the rat cortex *in vivo*. At illumination distances greater than 500 μm, 594-nm light was more effective than 532-nm light. Its superiority increased with distance. These results validate our prediction and highlight the significance of excitation-absorption trade-off in selecting illumination wavelength for optogenetics *in vivo*.

INTRODUCTION

Optogenetics has become an essential tool for clarifying the causal roles of genetically defined neuronal circuits in behavior (Tye and Deisseroth, 2012). The spatial volume in which a single optical fiber can manipulate neuronal activity has been reported to be ~1 mm^3 in rodents, with moderate light intensity (Gradinaru et al., 2009; Root et al., 2014). In macaque monkeys, however, considerably large brain volumes have been targeted with pharmacological suppression and lesion formation to induce behavioral changes (Goldman-Rakic, 1996; Squire et al., 2004). Therefore, to assess the brain functions by inducing comparable behavioral impacts in macaque monkeys using optogenetics, illumination of brain volume larger than 1 mm^3 would be necessary in most cases.

To efficiently manipulate a large brain volume with optogenetics, the opsin-expressing neurons, distant from the light source, need to be illuminated with a sufficient light intensity at an effective wavelength. However, high-power illumination could induce various off-target effects, primarily because of the heat generated by tissue-absorbed-light in the vicinity of the light source. These off-target effects include alteration of neuronal activity (Owen et al., 2019), vasodilation-related change in blood flow (Rungta et al., 2017), and heat-induced brain damage (Galvan et al., 2017). Therefore, technical modifications are required to enable neuronal activity modulation in a large volume with low-intensity illumination. One feasible strategy for circumventing this difficulty for *in vivo* opsin stimulation is to choose a light wavelength that satisfies the following two requirements: (1) efficient *in vivo* propagation in the brain tissue with reduced off-target effects and (2) effective excitation of the target opsin. To do so, the characteristics of each factor and their trade-off should be considered.

With regard to (1), the efficiency of light propagation along a distance is determined by scattering and absorption in the brain (Vo-Dinh T, 2003). In the adult brain with mature myelinated fibers, scattering contributes significantly. Light with longer wavelengths scatters less inside tissue and can propagate over longer distances. Various *in vitro* and *ex vivo* measurements and simulations have confirmed this property (Aravanis et al., 2007; Gysbrechts et al., 2016; Huber et al., 2008; Yaroslavsky, 2002; Yizhar et al., 2011). Although it is not taken into consideration in these studies, the chromophores are responsible for light absorption. The

[1]Department of Physiology, The University of Tokyo School of Medicine, Bunkyo-ku, Tokyo 113-0033, Japan

[2]Juntendo University, Graduate School of Medicine, Bunkyo-ku, Tokyo 113-8421, Japan

[3]Laboratory for Cognition Circuit Dynamics, RIKEN Center for Brain Science, Wako-shi, Saitama 351-0198, Japan

[4]Lead Contact

*Correspondence: rieko.setsuie@riken.jp

https://doi.org/10.1016/j.isci.2020.101276

absorbed light is converted to heat, which raises the tissue temperature (Arias-Gil et al., 2016; Shin et al., 2016; Stujenske et al., 2015), leading to off-target effects in the brain (Owen et al., 2019; Rungta et al., 2017). Various chromophore-containing molecules had been identified that contribute to the light absorption in the brain tissue. These include hemoglobin (Hb), lipofuscin, cytochrome, and eumelanin. Among them, Hb and lipofuscin are two of the major chromophore-containing molecules that crucially affect light absorption in the brain (Johansson, 2010). Lipofuscin is a complex composed of highly oxidized macromolecules. It cannot be degraded and accumulates mainly in the lysosome (Moreno-Garcia et al., 2018). Its light absorption peaks at around 300 nm and decreases drastically beyond 500 nm (Johansson, 2010). Around 60% of Hb is oxygenated *in vivo* and light absorption peaks at 415, 540, and 575 nm for oxy-Hb and at 435 and 555 nm for deoxy-Hb. At wavelengths longer than 575 nm, there is a drastic decrease in light absorption by oxy-Hb (Eggert and Blazek, 1987; Robles et al., 2010) (Figure 1A). The extent to which absorption contributes to the propagation of light in the brain, as compared with scattering, under a well-maintained blood flow condition, remains unclear (Aravanis et al., 2007; Azimipour et al., 2015; Johansson, 2010). However, recent *in vivo* studies (Acker et al., 2016; Azimipour et al., 2015) suggested that even the best reported previous *in vivo* measurement (Johansson, 2010) likely underestimated the absorption by Hb. Therefore, within 450–600 nm range, where light absorption by lipofuscin and Hb fluctuates drastically, the slightest shift in the illumination wavelength of light may significantly magnify the extent of light propagation, with reduced off-target effect (Figure 1A).

With regard to (2), we focused on Archaerhodopsin-T (ArchT), a light-driven proton pump, which is widely used to induce potent photoinhibition not only in rodents (Asok et al., 2018; Maier et al., 2015; Stefanik et al., 2013; Trouche et al., 2016; Tsunematsu et al., 2014; Wenker et al., 2017; Xu et al., 2016) but also in non-human primates (Afraz et al., 2015; Cavanaugh et al., 2012; Ohayon et al., 2013). *In vitro* spectral analyses of ArchT demonstrated its most effective excitation peak to be between 530 and 570 nm (Figure 1A) (Chuong et al., 2014; Han et al., 2011; Mattis et al., 2011). Therefore, most studies using ArchT, including the aforementioned studies, used 532 (Afraz et al., 2015; Asok et al., 2018; Cavanaugh et al., 2012; Maier et al., 2015; Ohayon et al., 2013; Wenker et al., 2017) or 561 nm light (Stefanik et al., 2013; Trouche et al., 2016) (Figure 1A). Unfortunately, the excitation spectrum of ArchT, including that of both the 532 and 561 nm light, largely overlaps with the absorption peak of Hb. However, the relatively wide spectrum of ArchT excitation suggests that ArchT can still be excited to over 80% of its excitation peak, i.e., to about 600 nm, which could avoid large absorbance by Hb (Figure 1A).

Taking factor (1) and (2) into consideration, we predicted that a wavelength of 594 nm would be more effective for ArchT-mediated large-volume optogenetic manipulation than the most conventionally used 532 nm light (Figure 1A). To directly test this prediction, it is essential to quantitatively measure the neural responses to light illuminated from different distances in the cortex where blood-related light-absorption remains stable. The optical responsiveness of individual neurons can vary depending on ArchT expression level, etc. Therefore, to obtain a reliable relationship between neuronal responses and light parameters (wavelength, power, and illumination distances), different wavelengths and illumination distances need to be measured in each recorded neuron. Such *in vivo* measurements have not been reported for any of the opsins to date.

In the present study, we quantitatively evaluated the effect of the light on the activity of ArchT-expressing neurons in the rat cortex *in vivo*. To validate our prediction, we selected a 594 nm laser as the light source, with a narrow spectral peak than light-emitting diodes (LEDs), and compared its results with those of a 532 nm laser (Figure 1A). We designed an adaptive electro-fiberoptic array, in which multiple side-emitting optical fibers were placed at different distances around one electrode, which enabled us to quantify the differential effects of light wavelengths, illuminated from multiple distances in the rat cortex.

RESULTS

Fabrication of the Electro-Fiberoptic Array

We designed our experiment so that the recorded neurons receive light from the light sources through the cortical areas with similar optical properties at multiple intracortical distances. White matter shows substantially higher light scattering than does gray matter. Thus, we focused on the light attenuation in the horizontal direction (i.e., parallel to the pial surface) but not in the vertical direction in the cortex, which minimized the confounding effects of white matter. To implement this design, we fabricated an electro-fiberoptic array that arranged a microelectrode and four optical fibers in parallel at defined distances. In this

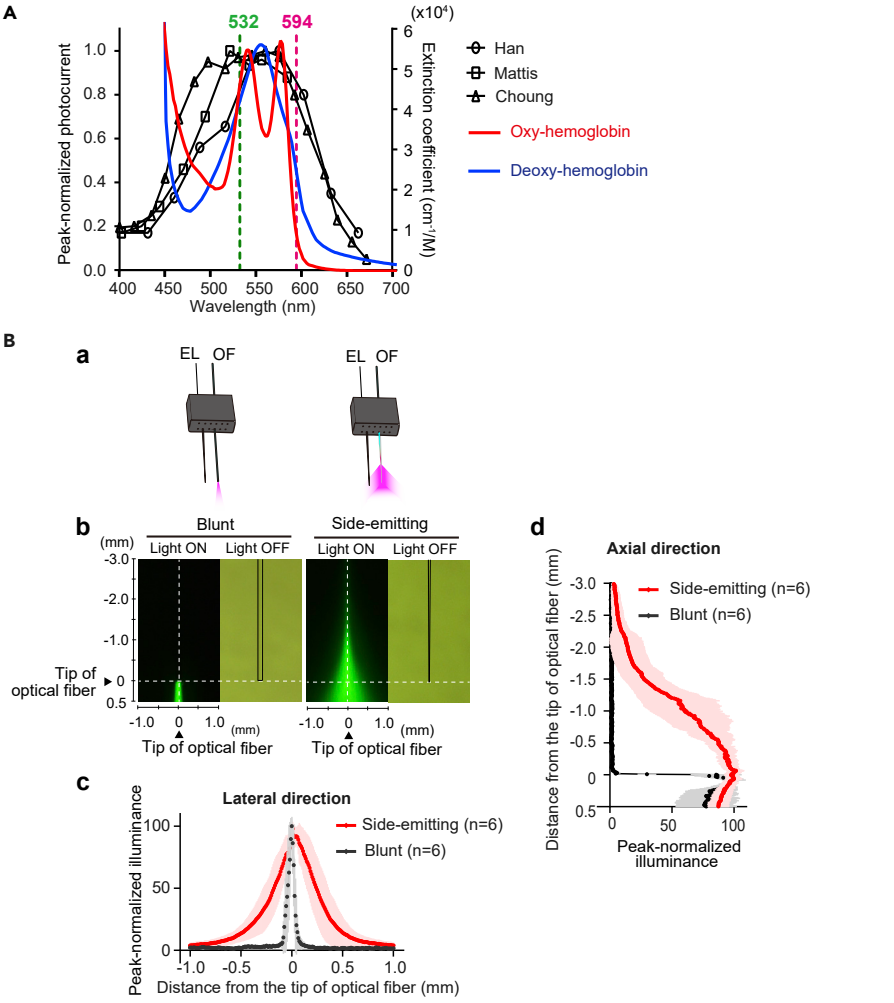
A
532
594
(x10⁴)
Peak-normalized photocurrent
Extinction coefficient (cm⁻¹/M)
Wavelength (nm)
Han
Mattis
Choung
Oxy-hemoglobin
Deoxy-hemoglobin
B
a
EL
OF
EL
OF
b
Blunt
Side-emitting
Light ON
Light OFF
Light ON
Light OFF
(mm)
Tip of optical fiber
Tip of optical fiber
Tip of optical fiber
c
Lateral direction
Side-emitting (n=6)
Blunt (n=6)
Peak-normalized illuminance
Distance from the tip of optical fiber (mm)
d
Axial direction
Side-emitting (n=6)
Blunt (n=6)
Distance from the tip of optical fiber (mm)
Peak-normalized illuminance
C
NeuN
ArchT-GFP
Merge
D
NeuN
ArchT-GFP
Merge

Figure 1. Wavelength-Dependent ArchT Excitation and Light Absorption by Hemoglobin, Illumination Properties of the Side-Emitting Optical Fiber, and ArchT-GFP Expression in Rat Cortex

(A) The 532 nm light and 594 nm light relative to the excitation spectra of ArchT *in vitro* measured by different groups (black) (Chuong et al., 2014; Han et al., 2011; Mattis et al., 2011), and the absorption spectrum of deoxy-hemoglobin (blue) and oxy-hemoglobin (red), which were modified based on the descriptions from (https://omlc.org/spectra/hemoglobin) (Schmitt, 1986; Takatani and Graham, 1979; Zijlstra et al., 1994).

(B) (a) Schematic image of the light illumination area (magenta) emitted from the tip of a blunt-end optical fiber (left) or the tapered surface of a side-emitting optical fiber (right). The electrode is placed in parallel with the optical fiber and the tip of the electrode is located within the light illumination area of the side-emitting optical fiber. EL, microelectrode; OF, optical fiber. (b) Representative image of light propagation by blunt-end and side-emitting optical fibers in fluorescein solution. The dotted lines in the images indicate the position of each fiber's tip (i.e., axial and lateral zero). Bright-field images of light-off condition are also shown. The border of the optical fibers in the bright-field image is visualized by tracing. (c and d) The mean illuminance of 473 nm light emitted from blunt-end (n = 6; gray) and side-emitting (n = 6; red) optical fibers in the lateral and the axial directions with the maximum illuminance at the fiber-tip normalized to 100. Shades denote the standard deviation (SD).

(C) Coronal image of a rat brain injected with the AAV vector (AAV5-CaMKIIa-ArchT-GFP) in the somatosensory area. Immunofluorescent staining for GFP (green), and a neuron marker NeuN (magenta). The scale bar indicates 1.0 mm.

(D) Confocal images of the ArchT expression area in (C). The white arrows indicate ArchT-GFP-expressing neurons. The level of GFP expression varies among the neurons. Most NeuN-positive neurons (magenta) are positive for ArchT-GFP (green). The scale bar indicates 50 μm.

See also Figure S1.

array, the electrode tip is horizontally spaced from the tip of the four optical fibers (see below, Figure 3A, and Transparent Methods "Fabrication of the electro-fiberoptic array" for details).

With blunt-end optical fibers, which are most commonly used in optogenetic experiments, the area of light emission is restricted to the facet of the optical fibers (see Transparent Methods "Analysis of the light emission properties of the side-emitting optical fibers" for the details of analysis). Unless several orders of magnitude higher input was applied, blunt-end optical fibers could not illuminate areas where electrode tip of our electro-fiberoptic array was placed (Figure 1Ba). Thus, we employed side-emitting optical fibers, which substantially enlarge the area of light illumination in the axial and lateral directions by extending the light-emitting surface toward the basal part of the optical fiber (Figure 1B) (Acker et al., 2016; Pisanello et al., 2017).

A representative image of light emission shows that the side-emitting optical fiber emitted light from its lateral surface along the axial direction of the optical fiber over 1.5 mm from the tip, with an increased angle of light emission (Figure 1Bb). The analysis of spatial illumination pattern demonstrated that the side-emitting optical fibers illuminated a significantly wider area compared with the conventional blunt-end optical fibers, in the axial and lateral direction (Figures 1Bc,d) (t test with Bonferroni corrections, n = 6 optical fibers, $p < 0.05$). This quantitative estimation is consistent with that of the previous reports (Acker et al., 2016; Pisanello et al., 2017).

Expression of ArchT-GFP in the Rat Cortex

We injected an adeno-associated virus vector encoding ArchT-GFP under the CaMKIIα promoter into the somatosensory area of rat cortex (Tsubota et al., 2015). Immunofluorescent double staining for GFP and a neuron-specific marker NeuN confirmed the selective expression with approximately 70% of ArchT-GFP in neurons (Figures 1C, D, and S1; see Transparent Methods "Immunofluorescent analysis of ArchT-GFP expression in the rat cortex" for details). To record unit activities during photostimulation, the electro-fiberoptic array was inserted in the cortical region, where ArchT-GFP expression was observed under a fluorescent stereomicroscope.

Relationship between Light Power and Suppression Efficacy of ArchT-Expressing Neurons *In Vivo*

The effects of photostimulation by two wavelengths of light need to be compared within the dynamic range of neuronal activity where the neuronal activity follows the modulation of the light power without saturation or insufficiency. Thus, we first explored such a dynamic range at a fixed distance (500 μm) for both wavelengths (Figure 2A). The activity of the same single/multi-unit was continuously recorded throughout a session in which we tested different light power. Suppression efficacy (supEff) is defined as [1 – (mean firing rate 1-s during the photostimulation)/(mean firing rate 1-s before the photostimulation)]. If

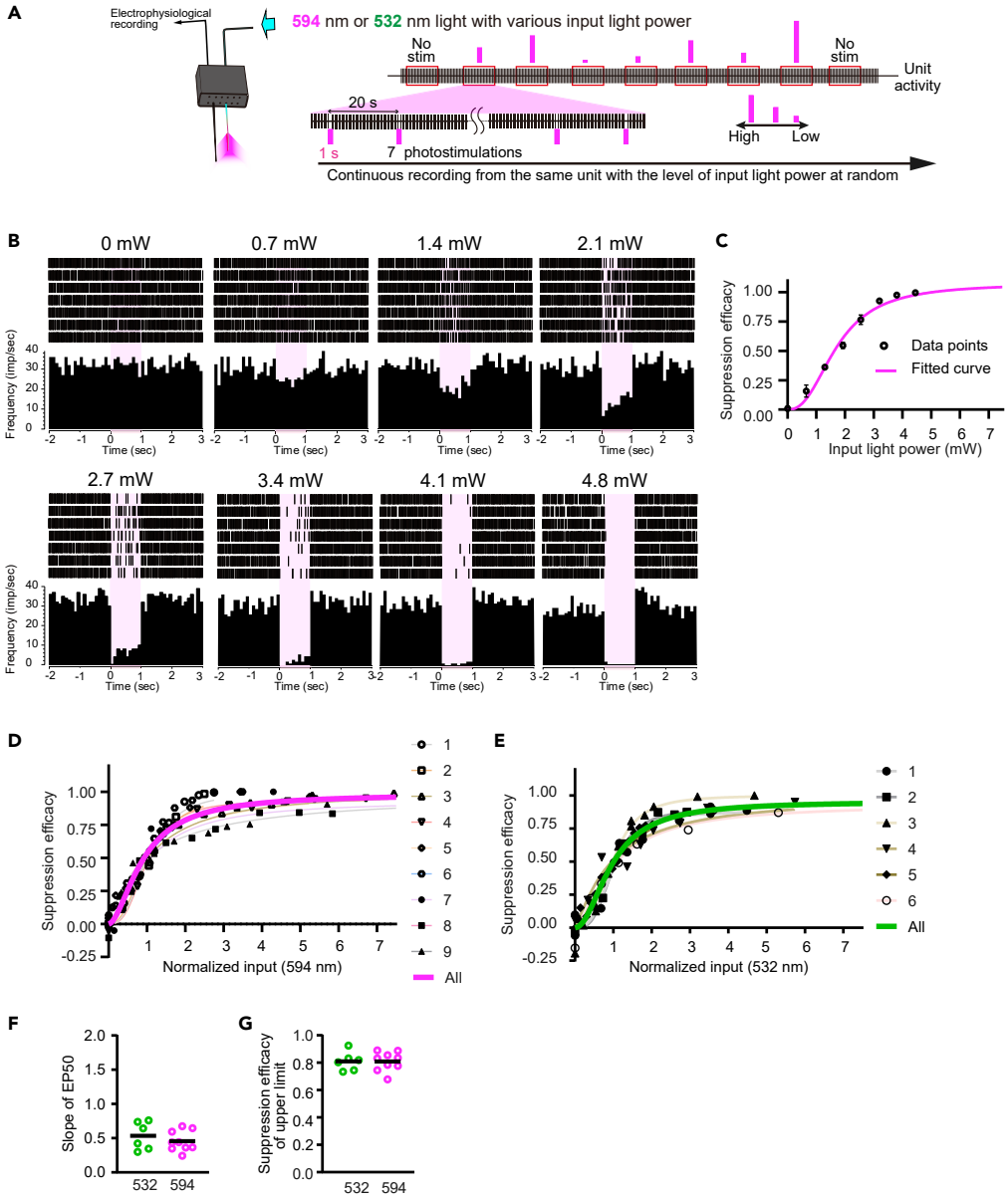

Figure 2. Relationships between the Suppression Efficacy of ArchT-Expressing Neurons and the Stimulation Light Power for 594 and 532 nm Light

(A) One microelectrode and one side-emitting optical fiber are placed at the distance of 500 μm from each other. The same single/multi-units were held throughout a single experiment to test the responses to different light powers emitted in a random order (single- and multi-units were recorded online with a time-voltage window discriminator; see Transparent Methods "Electrophysiological recording and optogenetic stimulation" for details). The height of the magenta line depicts the light power.

(B) Raster plots and peri-stimulus time histograms (PSTH) of a representative multi-unit tested for 594 nm light stimulation at eight different powers. The shaded area demarcates the stimulation period with 1-s continuous light illumination. The bin size is 100 ms.

(C) The relationship between light power and neuronal suppression efficacy (power-suppression curve) for the representative unit in (B). Suppression efficacy is defined as [1 – (mean firing rate 1-s during the photostimulation)/(mean firing rate 1-s before the photostimulation)]. If photostimulation induces no (or complete) suppression of the unit firing, the suppression efficacy value is 0 (or 1). The magenta trace represents a fitted curve estimated by logistic regression for the data from the unit ($\beta_{supEffmax} = 1$, $\beta_{inflection} = 3.23$, $\beta_{steepness} = 2.87$, $R^2 = 0.98$). (see Transparent Methods "Optogenetic data analysis" for an explanation of logistic regression coefficients).

Figure 2. *Continued*

(D) Power-suppression curves of different units for 594 nm photostimulation (n = 9 units; 3 single units and 6 multi-units). Light power is normalized to the half-maximum effective light power (EP50) for each unit. The magenta trace represents the power-suppression curve estimated by logistic regression for the data from all units ($\beta_{supEffmax}$ = 0.98, $\beta_{inflection}$ = 0.91, $\beta_{steepness}$ = 1.73, R^2 = 0.94).

(E) Power-suppression curves of different units for 532 nm photostimulation (n = 6 units; 2 single units and 4 multi-units). The green trace represents the power-suppression curve estimated by logistic regression for the data from all units ($\beta_{supEffmax}$ = 0.95, $\beta_{inflection}$ = 0.96, $\beta_{steepness}$ = 2.00, R^2 = 0.94).

(F) The slope of normalized EP50 from the power-suppression curves of each unit for 532 (n = 6) and 594 nm (n = 9). Values were obtained from individually fitted curves. Each dot represents the data from the fitted curve to each unit, and lines represent mean.

(G) Suppression efficacy of upper limit within the dynamic range of the power-suppression curves of each unit for 532 (n = 6) and 594 nm (n = 9). The values were obtained from individually fitted curves. Each dot represents the unit, and each line represents mean.

photostimulation induces no (or complete) suppression of the unit firing, the suppression efficacy value is 0 (or 1).

In a representative unit (Figure 2B), the firing rate decreased as the light power increased from 0 to 3.4 mW and remained nearly zero at 4.1 and 4.8 mW. The change in the activity of this unit as a function of the light power was fitted by logistic regression (the power-suppression curve; Figure 2C) (see Transparent Methods "Optogenetic data analysis" for details). To compare the power-suppression curves between two wavelength lights (6 and 9 units for 532 and 594 nm light, respectively), the mean $\beta_{supEffmax}$, $\beta_{steepness}$, and the statistical values for the goodness of fit to the logistic regression curve (R^2) were determined; for 594 nm light, $\beta_{supEffmax}$ 0.99 $\pm$ 0.0096 (mean $\pm$ SEM), $\beta_{steepness}$ 1.87 $\pm$ 0.21, R^2 0.96 $\pm$ 0.0100, and for 532 nm light, $\beta_{supEffmax}$ 0.95 $\pm$ 0.0220, $\beta_{steepness}$ 2.27 $\pm$ 0.37, R^2 0.97 $\pm$ 0.0085. The comparison of $\beta_{supEffmax}$, $\beta_{steepness}$, and R^2 values between 532 and 594 nm light did not show significant difference [$\beta_{supEffmax}$: t(13) = 1.52, p = 0.15, $\beta_{steepness}$: t(13) = 0.98, p = 0.34, R^2: t(13) = 0.32, p = 0.75]. Since the $\beta_{inflection}$ values naturally differ between the individual unit (2.58 $\pm$ 1.00 for 594 nm and 6.43 $\pm$ 1.86 for 532 nm), we normalized the different light powers in each unit by setting the light power to achieve the half-maximum-suppression (EP50) to 1 and estimated the power-suppression curves of the population data (magenta trace for 594 nm light, R^2 = 0.94, Figure 2D; green trace for 532 nm light, R^2 = 0.94, Figure 2E). The comparison of the slope of EP50 between 532 and 594 nm light also showed no significant difference [Figure 2F; t(13) = 1.52, p = 0.15 for supEff and t(13) = 0.86, p = 0.41 for the slope; two-tailed unpaired t test]. These results indicated that 532 and 594 nm light elicit indistinguishable power-suppression curves.

Then, we defined the effective dynamic range of supEff from 0 (lower limit) to the values of the point at which the slope of the power-suppression curve decreased to less than 0.1 (upper limit). The supEff values at the point were 0.81 $\pm$ 0.03 for the 532 nm light and 0.81 $\pm$ 0.02 for the 594 nm light [t(13) = 0.015, p = 0.99, two-tailed unpaired t test] (Figure 2G). These results ensured that we could reliably compare supEff by two light wavelengths with the same light power within this range of the suppression efficacy.

Suppression of ArchT-Expressing Neurons at Different Light Transmission Distances

We next compared the supEff between 532 and 594 nm light at four different transmission distances *in vivo*. Since the photosensitivity of individual neurons varies (indicated by the SEM for $\beta_{inflection}$ values as shown above; Mahn et al., 2018), the effect of different photoillumination conditions should be evaluated on the same neuron. To directly examine the effect of light transmission distance on the suppression of the same ArchT-expressing neurons, we placed one microelectrode and four side-emitting optical fibers at the horizontal distances of 250, 500, 700, and 1,000 μm in our electro-fiberoptic array (Figure 3A). This arrangement enabled us to measure the response of the same unit while changing the combination of distance from the light source and the illumination wavelengths (Figure 3A).

The units were recorded only when the neuronal activity of the unit could be completely suppressed by a brief preliminary qualitative testing. To compare the supEff between the two wavelengths, the light power was determined for each distance so that the firing of the unit is suppressed within its dynamic range. In a representative unit, we used the light power of 0.46, 1.3, 3.0, and 7.6 mW for the optical fibers at the distance of 250, 500, 700, and 1,000 μm, for both 532 and 594 nm light (Figure 3B). No-stimulation trials were interleaved between stimulation trials to ensure the stability of the firing rate and recovery from

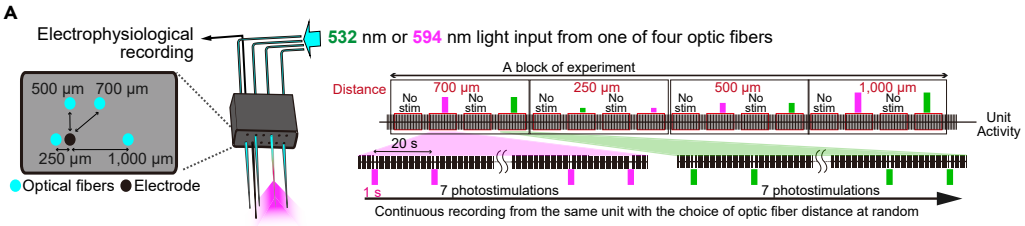
A
Electrophysiological recording
532 nm or 594 nm light input from one of four optic fibers
500 µm 700 µm
250 µm 1,000 µm
Optical fibers Electrode
A block of experiment
Distance
700 µm
250 µm
500 µm
1,000 µm
No stim
Unit Activity
20 s
1 s
7 photostimulations
7 photostimulations
Continuous recording from the same unit with the choice of optic fiber distance at random

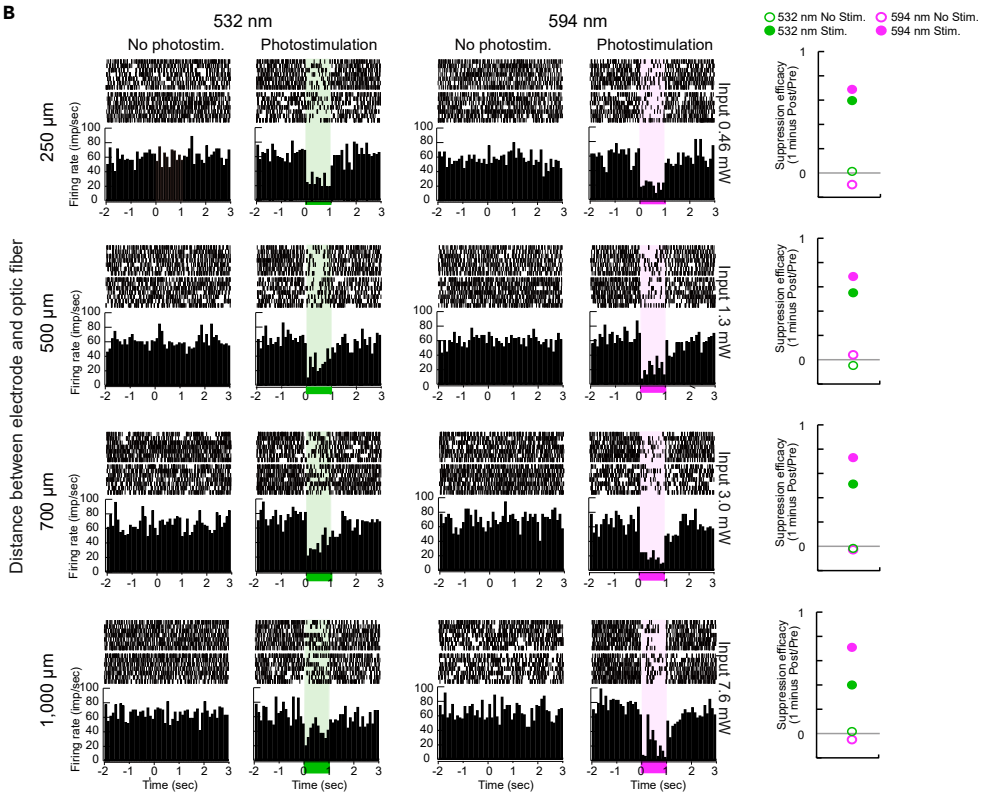
B
532 nm
594 nm
No photostim.
Photostimulation
532 nm No Stim.
532 nm Stim.
594 nm No Stim.
594 nm Stim.
Distance between electrode and optic fiber
250 µm
500 µm
700 µm
1,000 µm
Firing rate (imp/sec)
Input 0.46 mW
Input 1.3 mW
Input 3.0 mW
Input 7.6 mW
Suppression efficacy (1 minus Post/Pre)
Time (sec)

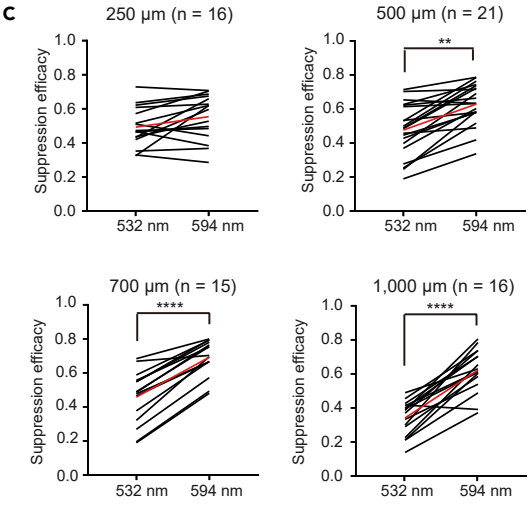
C
250 µm (n = 16)
500 µm (n = 21)
700 µm (n = 15)
1,000 µm (n = 16)
Suppression efficacy
532 nm
594 nm
**
****

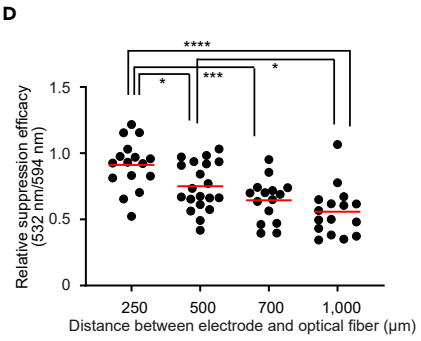
D
Relative suppression efficacy (532 nm/594 nm)
Distance between electrode and optical fiber (µm)
250
500
700
1,000
*
***
****

Figure 3. Comparison of the Suppression Efficacy between 532 nm Light and 594 nm Light at Four Different Distances

(A) The electro-fiberoptic array is configured so that the side-emitting optical fibers are placed at a distance of 250, 500, 700, and 1,000 μm from the microelectrode. The same single/multi-unit was maintained throughout a single experiment to test the responses to different distances and wavelengths (see Transparent Methods "Electrophysiological recording and optogenetic stimulation" for details on how we defined the unit online). The height of the magenta line depicts the light power (see Transparent Methods "Electrophysiological recording and optogenetic stimulation" for how we determined the light power for each distance).

(B) Photostimulation by 532 and 594 nm light. Left, raster plots and PSTHs of a representative unit by 532 or 594 nm photostimulation at four different distances. Stimulated and non-stimulated trials were interleaved. The shaded area demarcates the stimulation period with 1-s continuous light illumination. Bin size is 100 ms. Right, the graphs represent the suppression efficacy for 532 and 594 nm light at different distances.

(C) Population suppression efficacy of 532 and 594 nm light at different distances. The black lines indicate individual units and the red lines indicate the mean of the units [two-way ANOVA: distance, $F(3,82) = 4.42$, $p = 0.0062$; wavelength, $F(1, 46) = 40.50$, $p < 0.0001$; distance * wavelength, $F(3, 82) = 6.89$, $p = 0.0003$; followed by Bonferroni's multiple comparisons, $p = 0.56$, $p = 0.0007$, $p < 0.0001$, $p < 0.0001$ for 250 μm ($n = 16$; 4 single- and 12 multi-units), 500 μm ($n = 21$; 5 single- and 16 multi-units), 700 μm ($n = 15$; 3 single- and 12 multi-units), and 1,000 μm ($n = 16$; 4 single- and 12 multi-units) respectively, $^{**}p < 0.005$, $^{****}p < 0.0001$].

(D) Relative suppression efficacy between 532 and 594 nm light at different distances. The relative suppression efficacy for each unit is the ratio of the suppression efficacy between 532 and 594 nm light at each distance. The circles indicate individual units, and the red lines indicate the average [one-way ANOVA; distance, $F(3, 63) = 11.59$, $p < 0.0001$; followed by Tukey-Kramer multiple comparisons, $^{*}p < 0.05$, $^{***}p < 0.0005$, and $^{****}p < 0.0001$].

See also Figures S2 and S3.

the previous stimuli. In this unit, the results of two recording blocks were averaged into one peri-stimulus time histograms (PSTHs) (Figure 3B). This representative unit showed stronger suppression with 594 nm light than with 532 nm light as the distance increased (Figure 3B, right graph). Population data showed a consistent result (Figure 3C) [two-way ANOVA; main effect of distance, $F(3, 82) = 4.42$, $p = 0.0062$; main effect of wavelength, $F(1, 46) = 40.50$, $p < 0.0001$; interaction between distance and wavelength, $F(3, 82) = 6.89$, $p = 0.0003$]. At 250 μm, the suppression efficacy did not show a difference between the two wavelengths. However, at 500 μm, the 594 nm light began to show a larger suppression efficacy than did the 532 nm light, and the difference is also observed at 700 and 1,000 μm [Bonferroni's multiple comparisons after two-way ANOVA, $p = 0.56$ ($n = 16$, 250 μm), $p = 0.0007$ ($n = 21$, 500 μm), $p < 0.0001$ ($n = 15$, 700 μm), $p < 0.0001$ ($n = 16$, 1,000 μm)].

To compare the distance-dependent changes of the suppression efficacy between the two wavelengths, we plotted the relative suppression efficacy between two wavelengths against the distance (Figure 3D). The relative suppression efficacy showed a significant decrease with distance [$F(3, 63) = 11.59$, $p < 0.0001$, one-way ANOVA]. The relative suppression efficacy was significantly smaller at 500, 700, and 1,000 μm compared with that at 250 μm ($p = 0.044$, $p = 0.0006$, $p < 0.0001$ respectively, Tukey-Kramer post hoc test after one-way ANOVA) and was significantly smaller at 1,000 μm than that at 500 μm ($p = 0.011$). The relative suppression efficacy was 0.91 ± 0.05 (mean ± SEM) at 250 μm but decreased to 0.53 ± 0.05 at 1,000 μm, indicating that the 594 nm light is about twice more effective than the 532 nm light at 1,000 μm (Figure 3D).

Although the quantitative analyses can be best performed at the light intensity within the dynamic range, as shown above, the analysis of data including those outside the dynamic range replicated the results of Figures 3C and 3D (Figures S2A and S2B). We also examined single-unit data sorted offline (Figures S3A–S3E; see Transparent Methods "Sorting and analysis of single-unit" for the offline-sorting procedure). The results with single-unit data (Figures S3F and S3G) replicated those with single/multi-unit data (Figures 3C and 3D).

To confirm that light stimulus itself does not affect the activity of non-ArchT-expressing neurons, we conducted a separate experiment and recorded neuronal activities at the cortex of naive rats. The results confirmed that, within the light intensity range we used in the experiments with the ArchT-expressing rats, neither 532 nor 594 nm light changed the neuronal activity of non-ArchT-expressing neurons [two-way ANOVA: main effect of light, $F(1, 7) = 2.47$, $P = 0.16$; main effect of wavelength, $F(1, 7) = 0.188$, $p = 0.68$; interaction between light and wavelength, $F(1, 7) = 1.31$, $p = 0.29$] (Figure S2C).

Next, we compared the relative input light power to equally suppress the neural firing of ArchT-expressing neurons among different wavelengths and distances by estimating the relative EP50 values for each condition (Figure 4A; see Transparent Methods "Optogenetic data analysis" for details). The required relative input light power [Exp-data (firing)] increased with distance; this was significantly different between the two wavelengths, and the difference increased with distance [two-way ANOVA; main effect of distance, $F(3, 48) = 49.61$, $p < 0.0001$; main effect of wavelengths, $F(1, 16) = 5.08$, $p = 0039$; interaction between distance and wavelength, $F(3, 48) = 5.04$, $p = 0.0041$]. At a distance of 1,000 μm, the estimated EP50 of 594 nm light was significantly smaller than that of 532 nm light [$p = 0.0003$ ($n = 9$), Bonferroni's multiple comparisons after two-way ANOVA] (Figure 4A). When the distance of illumination expanded 4-fold (from 250 to 1,000 μm), the estimated light power needed to suppress the same unit was increased 21.0-fold with 532 nm light, but the increase remained at only 11.4-fold with 594 nm light. Convergingly, photostimulation by the 594 nm light is estimated to require only 54% of the light power, compared with photostimulation by the 532 nm light at the distance of 1,000 μm.

Finally, we simulated the light propagation from a side-emitting optical fiber in the brain and compared the simulated results with the experimental data. Specifically, we conducted a random-walk Monte Carlo simulation of photon packets (see Transparent Methods "Monte Carlo simulation" for details) (Pisanello et al., 2017; Sileo et al., 2018; Stujenske et al., 2015) to estimate the light propagation in the brain. The simulation requires a set of three input parameters: scattering coefficients [$\mu_s(\lambda)$] (λ = wavelength), absorption coefficients [$\mu_a(\lambda)$], and anisotropy factors [$\mu_{af}(\lambda)$]. We simulated light propagation by using the following three sets of parameters. In the first simulation (J-model), we applied a set of parameters obtained experimentally *in vivo* by Johansson (2010). The Johansson's absorption coefficients are known to lack the contribution of absorption by oxy-Hb and to represent the absorption by a partial amount of deoxy-Hb (Johansson, 2010). In the second simulation (woJ-model), $\mu_a(\lambda)$ was set to 0, along with the same $\mu_s(\lambda)$ and $\mu_{af}(\lambda)$ as those in J-model. Thus, in this woJ-model, we simulated the light propagation by considering only the scattering in the brain tissue. In the third simulation (Exp-model), $\mu_a(\lambda)$ was estimated to fit the light propagation patterns obtained from our experimental data [the Exp-data (light); see Transparent Methods "Monte Carlo Simulation" for details] along with the same $\mu_s(\lambda)$ and $\mu_{af}(\lambda)$ as those in J-model. Based on these simulations (Figure S4), we calculated the relative input light power required to deliver equal light power at the distances of 250, 500, 700, and 1,000 μm from the tip of the optical fiber in the lateral direction with 532 and 594 nm (Figure 4B). The differences in relative input light power between 532 and 594 nm light within each dataset were also plotted (inset Figure 4B). The comparison between the experimental data [Exp-data (light)] and the simulation results of woJ-model and J-model provided evidence that the light absorption by Hb is responsible for the superiority of 594 nm light to 532 nm light in suppressing the activity of ArchT-expressing neurons (for further details, see Figure 4 Legend and Discussion). The comparison also demonstrated that the contribution of scattering is smaller compared with that of absorption, in the lateral direction of light propagation.

DISCUSSION

In the present study, we directly compared the suppression efficacy of 532 and 594 nm light at multiple illuminating distances by developing an electro-fiberoptic array with multiple side-emitting optical fibers. The 594 nm light was found to be 2-fold more effective than 532 nm light to silence ArchT-expressing neurons through an intracortical distance of 1,000 μm. The 594 nm light was slightly off the excitation plateau and largely off the peak of the Hb absorption spectrum, whereas the 532 nm light falls within the excitation peak and on the peak of the Hb absorption spectrum. This result provided direct positive evidence for our prediction that 594 nm light is more effective than the conventionally used 532 nm light for silencing ArchT-expressing neurons *in vivo*. In addition, a comparison between the results obtained from the simulation of light propagation in the brain and our experimental data demonstrated that light absorption by Hb is responsible for the difference observed between 532 and 594 nm light. This result also supports our premise that light absorption by Hb should have a greater influence on light propagation than previously estimated, particularly in the lateral direction of light propagation. Our results highlighted the general importance of considering both the wavelength dependence of the opsin's excitation spectrum *in vitro* and the absorption of light *in vivo*. We call it an excitation-absorption trade-off.

Previous measurements of *in vivo* light propagation (Acker et al., 2016; Johansson, 2010) suggested that the absorption of light by the chromophore-harboring molecules, especially the Hb in the blood (Mahn et al., 2018), had been greatly underestimated. In the present study, we directly compared the responses

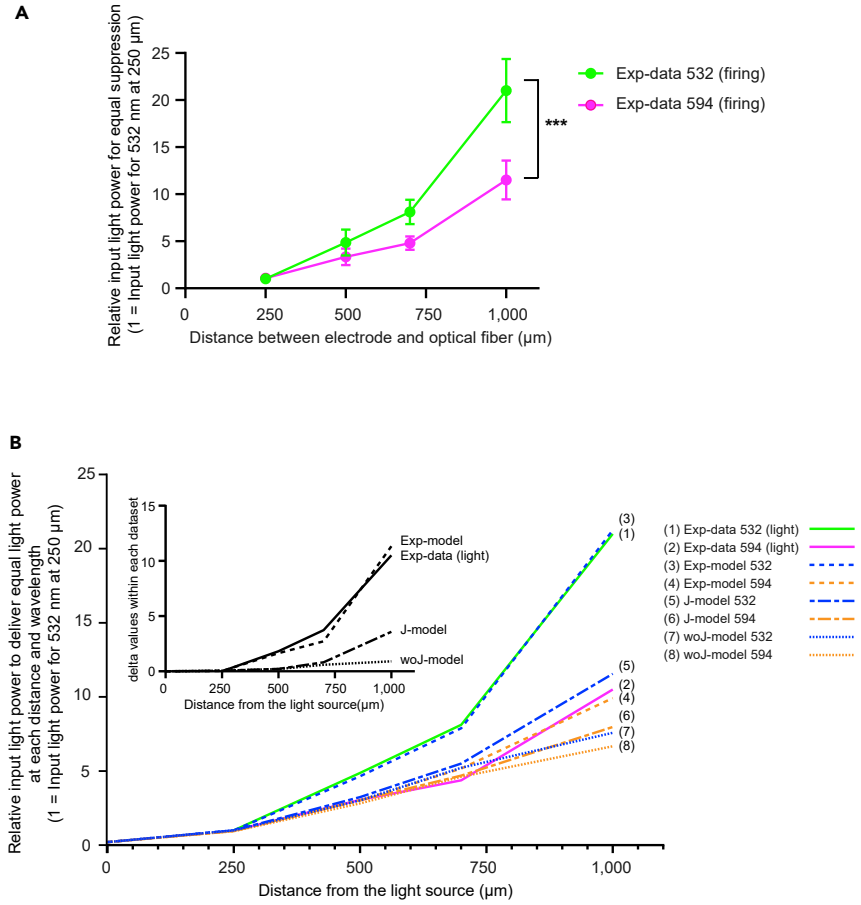

Figure 4. Input Light Power Required for Equivalent Neural Suppression between 532 and 594 nm *In Vivo* and Comparison between the Simulation Results and the Experimental Data

(A) Estimated relative input light power (EP50) required to induce half-maximum suppression for 532 nm light [Exp-data 532 (firing), green] and 594 nm light [Exp-data 594 (firing), magenta], at the distances of 250, 500, 700, and 1,000 μm. The estimated EP50 was normalized to the value of 532 nm at 250 μm. The circles indicate the mean of 9 units. The error bar denotes the SEM [two-way ANOVA: distance, $F(3, 48) = 49.61$, $p < 0.0001$; wavelength, $F(1, 16) = 5.08$, $p = 0.039$; distance × wavelength, $F(3, 48) = 5.04$, $p = 0.0041$; ***$p < 0.0005$, post hoc Bonferroni's multiple comparisons].

(B) Computationally estimated input light power required to deliver equal light power at the distance of 250, 500, 700, and 1,000 μm using a Monte Carlo simulation (see Figure S4; Transparent Methods "Monte Carlo simulation" for details). The model in the Monte Carlo simulation is defined by a set of three input parameters: scattering coefficients [$\mu_s(\lambda)$], absorption coefficients [$\mu_a(\lambda)$], and anisotropy factors [$\mu_{af}(\lambda)$]. In the first simulation model [J-model: (5), (6)], we applied a set of input parameters obtained *in vivo* by Johansson (2010). The Johansson's $\mu_a(\lambda)$ are known to lack the contribution from absorption by oxy-hemoglobin and, partially, by deoxy-hemoglobin (Johansson, 2010). In the second simulation model [woJ-model: (7), (8)], $\mu_a(\lambda)$ were set to 0, along with the same $\mu_s(\lambda)$ and $\mu_{af}(\lambda)$ as those in J-model. With woJ-model, we simulated the light propagation by considering only the spatially non-homogeneous light scattering in the brain tissue. In the third simulation model [Exp-model: (3), (4)], $\mu_a(\lambda)$ was estimated to properly capture the trajectory of light propagation patterns of the Exp-data (light) (see Transparent Methods "Monte Carlo simulation" for details) along with the same $\mu_s(\lambda)$ and $\mu_{af}(\lambda)$ as those in J-model [note that the plots for the Exp-model almost overlapped with those for the Exp-data (light) at both 532 and 594 nm light, suggesting that the estimation of $^{Exp}\mu_a(\lambda)$ values is valid]. The estimated input light power was normalized to the value of 532 nm at 250 μm in each model. The experimental data [Exp-data (light): (1), (2)] was also plotted, whose values were linearly converted from the [Exp-data (firing)] values in (A) by using the ArchT excitation efficiency values at 532 and 594 nm light that were obtained from ArchT excitation spectrum in Figure 1A (see Transparent Methods "Optogenetic data analysis" for details). The inset figure in (B) represents the differences in relative input light power (delta values in relative input light power) between 532 and 594 nm light at each distance within the dataset.

See also Figure S4.

of ArchT-expressing neurons with 532 and 594 nm light illumination using DPSS lasers, whose spectral widths are narrower than LEDs, under precise control of input light power. Based on our neurophysiological measurements, we demonstrated that 594 nm light required only 50% of the power required by 532 nm light to achieve an equivalent suppression at a distance of 1,000 μm (Figure 4A). The present *in vivo* observation cannot be directly predicted from the excitation spectrum of ArchT measured *in vitro*, where the largest photocurrents are observed at 530–560 nm (Chuong et al., 2014; Han et al., 2011; Mattis et al., 2011) (Figure 1A).

The efficiency of light propagation along a distance is determined by scattering and absorption in the brain. Light with longer wavelengths scatters less inside tissue and can propagate over longer distances. Various chromophore-harboring molecules are responsible for light absorption in the brain, such as Hb and lipofuscin. To determine which of these factors are mainly responsible for the observed differences between 532 and 594 nm light, we compared the experimental results [Exp-data (light)] with the results obtained from the Monte Carlo simulations (woJ-model and J-model; Figure 4B). The woJ-model reflected only the scattering, and J-model reflected both the scattering and the absorption, although the absorption by the Hb might only partially be reflected (Johansson, 2010). In contrast to J-model, Exp-data (light) fully reflected the light absorption, including that by Hb. Therefore, the comparisons in Figure 4B suggested the following two conclusions: (1) The scattering is responsible for the difference between 532 and 594 nm light; however, its contribution is predicted to be relatively small in the lateral direction of light propagation. (2) The absorption by Hb would be mainly responsible for the difference between 532 and 594 nm light observed in this study.

To quantitatively support the above conclusion, we further estimated the absorption coefficients for Exp-data (light) [$^{Exp}\mu_a(\lambda)$] [note that Exp-model is the result of applying $^{Exp}\mu_a(\lambda)$ for simulation] [see Transparent Methods "Estimation of the absorption coefficients for Exp-data (light) " for details], as well as the partial absorption coefficients of Hb for Exp-data (light) [$^{Exp}\mu_{a,Hb}(\lambda)$] at both 532 and 594 nm [see Transparent Methods "Estimation of the partial absorption coefficients of Hb for Exp-data (light) " for details]: $^{Exp}\mu_a(532) = 0.392\ mm^{-1}$, $^{Exp}\mu_a(594) = 0.234\ mm^{-1}$; $^{Exp}\mu_{a,Hb}(532) = 0.248\ mm^{-1}$, $^{Exp}\mu_{a,Hb}(594) = 0.159\ mm^{-1}$. The ratio of the Hb contribution to the total light absorption was larger than 0.6 for both wavelengths. Moreover, the contribution of Hb was larger than the contribution of the rest of the chromophore-harboring molecules to the difference in light absorption between 532 and 594 nm. Although $^{Exp}\mu_{a,Hb}(\lambda)$ was smaller than theoretically predicted at both 532 and 594 nm (see Transparent Methods "Estimation of the partial absorption coefficients of Hb for Exp-data" for details), the results suggested that, among all of the chromophore-harboring molecules present, Hb is the primary component contributing to light absorption at both wavelengths and Hb would be the main factor responsible for the differences observed between 532 and 594 nm light in our experimental data. Altogether, our results underscored the general importance of considering both the wavelength dependence of the opsin's excitation spectrum *in vitro* and the absorption of light primarily by Hb *in vivo*.

In this study, we evaluated the effects of distance changes in the lateral direction, but not in the vertical direction, to avoid the interference from the white matter. The light propagation patterns in the vertical direction of Exp-model in Figure S4, as well as the ratio (532 nm/594 nm = 1.1) of the estimated relative light input power to deliver equal light power at 1,000 μm in the vertical direction from the tip of the optical fiber in this model, suggest that the superiority of 594 nm light over 532 nm light in light propagation in the vertical direction is not as prominent as in the lateral direction (the ratio is 2.1; Figure 4B).

In addition to the decrease of light propagation, light absorption has been considered to be responsible for various off-target effects. Owen et al. (2019) demonstrated that, in wild-type mice without opsin expression, continuous 1-s illumination of 532 nm light at 15 mW could induce significant suppression of neuronal activity resulting in a behavioral change, presumably due to the heat generated from the absorbed light. Rungta et al. (2017) demonstrated that light with wavelengths between blue and red with illumination parameters of 20-ms pulse width, 20 Hz, 5 mW, 2-s duration could cause an off-target effect on vasodilation and the magnitude of such vasodilation decreased with increasing wavelength. This photo-vasodilation could affect the blood-oxygen-level-dependent (BOLD) signals of functional MRI. Hb being the primary molecule responsible for light absorption *in vivo*, it is likely that these phenomena are induced by the heat generated from the light absorbed by Hb. Although we did not directly measure temperature changes in this study, Shin et al. (2016) measured brain temperature *in vivo* and reported that illumination with

532 nm light causes a prominent rise in temperature compared with that by 594 nm light. Since we observed comparable suppression between the illumination of 532 and 594 nm light at the closest distance of 250 μm, 594 nm light might be preferable over 532 nm light to suppress a small brain area as well as and to minimize the off-target effects due to the heat generated by the absorbed light.

To expand the spatial volume of optogenetic manipulation, efforts have been made along several lines of strategy such as (1) increasing the light-emitting surface area and/or sites of the light-emitting optical fibers, (2) selecting a wavelength with superior propagation and reduced off-target effects in the brain, (3) modifying opsin proteins to improve its sensitivity to light, and (4) enhancing the amount of opsins to be expressed without side effects. The findings of the present study contribute to strategy (2). For strategy (1), various novel implementations have been applied (for the review see Galvan et al., 2017). For example, Tamura et al. (2012) developed a glass-coated optrode that can linearly arrange four sharpened optical fibers and activate a sufficient number of ChR2-expressing neurons in the perirhinal cortex of macaque monkeys, which drastically shifted their recognition judgment of visual objects (Tamura et al., 2017). In the present study, we used side-emitting optical fibers to assemble the electro-fiberoptic array. This side-emitting optical fiber substantially expanded the photoillumination area, both laterally and axially [strategy (1), Figure 2A], as reported previously (Acker et al., 2016; Pisanello et al., 2017). Our glass-etching protocol to render side emission of light does not use the toxic chemical, hydrofluoric acid, and is applicable in all laboratory settings. For strategy (3), some opsins have been modified to enhance light sensitivity by accumulating the opsin proteins in the open state (step function variants; Bamann et al., 2010; Berndt et al., 2009; Yizhar et al., 2011) and other opsins have been modified to enable excitation by longer wavelength light, including red-shifted opsins such as Chrimson and Jaws (Chuong et al., 2014; Inoue et al., 2019; Klapoetke et al., 2014). Jaws was used in macaques, which significantly disrupted the memory-guided saccade of macaques (Acker et al., 2016). Strategy (4) has been reviewed elsewhere (Kim et al., 2017; Mattis et al., 2011).

The combination of our side-emitting optical fibers, ArchT, and the use of 594 nm light, which avoids absorption by Hb, provides a promising strategy for large-scale optogenetic silencing in non-human primates. It can enable milli-second-level manipulation of the neural circuits for high-level assessment of cognitive/metacognitive behaviors, previously verified by a pharmacological intervention (Miyamoto et al., 2017, 2018).

Limitation of the Study

There are several opsins, besides ArchT, whose excitation peak overlaps fully or partially with the absorption spectrum of Hb, such as the red-shifted channelrhodopsins (VChR1, V1C1, ChrimsonR, ReaChR, etc.) (Kim et al., 2017) and chloride channelrhodopsins (GtACR1, mdGtACR2, PsChR1, PaACR1, etc.) (Wiegert et al., 2017). The implications of our study on the strategy for manipulating neuronal activities over a wide brain area with minimal off-target effects may also be applicable to these opsins.

For example, the optimal wavelength for eNpHR3 is reported at around 570 nm (Tye, 2011). Even though the effect of light absorption by deoxy-Hb is relatively small at 570 nm, it disappears at wavelengths longer than 600 nm. The effect of scattering is also smaller at wavelengths longer than 600 nm. Thus, we suppose that illumination of light at around 600 nm may be optimal for suppressing neuronal activities of a wider brain area when using eNpHR3, according to the "excitation-absorption trade-off. " Note that Jaws, a red-shifted halorhodopsin, is also suited for 600-nm excitation.

The optimal wavelength for GtACR1 is reported at around 520 nm (Govorunova et al., 2015). At the proximity of 520 nm, light absorption both by lipofuscin and Hb could limit light propagation within the brain *in vivo* because their absorption peaks are located at 300–500 and 530–570 nm, respectively. The excitation-absorption trade-off suggests that we could experimentally determine the optimal wavelength of light to illuminate GtACR1 in the brain *in vivo* by comparing the suppression efficacies between 520 nm and around 600 nm, as we have demonstrated in the present study with ArchT. We also note that, as GtACR1 is an inhibitory anion-conducting channelrhodopsin, pulsed illumination is sufficient to induce its activation, which is different from pump-type inhibitory opsins, including ArchT and eNpHR3, which require continuous illumination. Pulsed illumination allows us to use a relatively high intensity of light (Owen et al., 2019) as compared with continuous illumination that we used in our experiments with ArchT. In fact, 635 nm light was used to suppress the activity of distant GtACR1-expressing neurons *in vivo* with the relatively high light intensity illumination (Li et al., 2019).

As shown above, because different opsins harbor different excitation peaks, our result with ArchT cannot be applied directly to other opsins. Therefore, a preferable stimulation wavelength for *in vivo* application should be examined based on the excitation-absorption trade-off and experimentally determined for each opsin by direct measurement of neuronal activity, as reported in this study.

Resource Availability

Lead Contact

Further information and requests for resources and reagents should be directed to and will be fulfilled by the Lead Contact, Rieko Setsuie (rieko.setsuie@riken.jp).

Materials Availability

This study did not generate new materials. Detailed information on how we fabricated the electro-fiberoptic array can be found in the accompanying Transparent Methods supplemental file.

Data and Code Availability

This study did not generate a new code. All relevant data are available from the Lead Contact upon reasonable request.

METHODS

All methods can be found in the accompanying Transparent Methods supplemental file.

SUPPLEMENTAL INFORMATION

Supplemental Information can be found online at https://doi.org/10.1016/j.isci.2020.101276.

ACKNOWLEDGMENTS

We thank F. Pisanello (Istituto Italiano di Tecnologia, Center for Biomolecular Nanotechnologies) for sharing the OpticStudio script and the MATLAB script. We thank T. Osada and T. Watanabe-Fukui for their technical assistance. This work was supported in part by MEXT/JSPS KAKENHI grants 17H06161 to Y.M., 17K07062, 18H04953, 18H05140, to M.T., and 19K06949 to R.S., The Uehara Memorial Foundation to M.T., JSPS Fellowships for Research Abroad and for Young Scientists to K.M. (265926) and K.T. (280123), Brain Science Foundation, The Ichiro Kanehara Foundation, and Research Foundation for Opto-Science and Technology to K.T.

AUTHOR CONTRIBUTIONS

R.S. and K.T. conducted the experiments; R.S., K.T., and Y.M. designed the experiments; T.W. conducted the simulations; R.S., K.T., and K.M. analyzed the data; and R.S., K.T., K.M., M.T., T.W., and Y.M. wrote the paper.

DECLARATION OF INTERESTS

The authors declare no competing financial interests.

Received: December 4, 2019
Revised: March 23, 2020
Accepted: June 11, 2020
Published: July 24, 2020

REFERENCES

Acker, L., Pino, E.N., Boyden, E.S., and Desimone, R. (2016). FEF inactivation with improved optogenetic methods. Proc. Natl. Acad. Sci. U S A *113*, E7297–E7306.

Afraz, A., Boyden, E.S., and DiCarlo, J.J. (2015). Optogenetic and pharmacological suppression of spatial clusters of face neurons reveal their causal role in face gender discrimination. Proc. Natl. Acad. Sci. U S A *112*, 6730–6735.

Aravanis, A.M., Wang, L.P., Zhang, F., Meltzer, L.A., Mogri, M.Z., Schneider, M.B., and Deisseroth, K. (2007). An optical neural interface: in vivo control of rodent motor cortex with integrated fiberoptic and optogenetic technology. J. Neural Eng. *4*, S143–S156.

Arias-Gil, G., Ohl, F.W., Takagaki, K., and Lippert, M.T. (2016). Measurement, modeling, and prediction of temperature rise due to optogenetic brain stimulation. Neurophotonics *3*, 045007.

Asok, A., Draper, A., Hoffman, A.F., Schulkin, J., Lupica, C.R., and Rosen, J.B. (2018). Optogenetic silencing of a corticotropin-releasing factor

pathway from the central amygdala to the bed nucleus of the stria terminalis disrupts sustained fear. Mol. Psychiatry *23*, 914–922.

Azimipour, M., Atry, F., and Pashaie, R. (2015). Effect of blood vessels on light distribution in optogenetic stimulation of cortex. Opt. Lett. *40*, 2173–2176.

Bamann, C., Gueta, R., Kleinlogel, S., Nagel, G., and Bamberg, E. (2010). Structural guidance of the photocycle of channelrhodopsin-2 by an interhelical hydrogen bond. Biochemistry *49*, 267–278.

Berndt, A., Yizhar, O., Gunaydin, L.A., Hegemann, P., and Deisseroth, K. (2009). Bi-stable neural state switches. Nat. Neurosci. *12*, 229–234.

Cavanaugh, J., Monosov, I.E., McAlonan, K., Berman, R., Smith, M.K., Cao, V., Wang, K.H., Boyden, E.S., and Wurtz, R.H. (2012). Optogenetic inactivation modifies monkey visuomotor behavior. Neuron *76*, 901–907.

Chuong, A.S., Miri, M.L., Busskamp, V., Matthews, G.A., Acker, L.C., Sorensen, A.T., Young, A., Klapoetke, N.C., Henninger, M.A., Kodandaramaiah, S.B., et al. (2014). Noninvasive optical inhibition with a red-shifted microbial rhodopsin. Nat. Neurosci. *17*, 1123–1129.

Eggert, H.R., and Blazek, V. (1987). Optical properties of human brain tissue, meninges, and brain tumors in the spectral range of 200 to 900 nm. Neurosurgery *21*, 459–464.

Galvan, A., Stauffer, W.R., Acker, L., El-Shamayleh, Y., Inoue, K.I., Ohayon, S., and Schmid, M.C. (2017). Nonhuman primate optogenetics: recent advances and future directions. J. Neurosci. *37*, 10894–10903.

Goldman-Rakic, P.S. (1996). The prefrontal landscape: implications of functional architecture for understanding human mentation and the central executive. Philos. Trans. R. Soc. Lond. B Biol. Sci. *351*, 1445–1453.

Govorunova, E.G., Sineshchekov, O.A., Janz, R., Liu, X., and Spudich, J.L. (2015). NEUROSCIENCE. Natural light-gated anion channels: a family of microbial rhodopsins for advanced optogenetics. Science *349*, 647–650.

Gradinaru, V., Mogri, M., Thompson, K.R., Henderson, J.M., and Deisseroth, K. (2009). Optical deconstruction of parkinsonian neural circuitry. Science *324*, 354–359.

Gysbrechts, B., Wang, L., Trong, N.N., Cabral, H., Navratilova, Z., Battaglia, F., Saeys, W., and Bartic, C. (2016). Light distribution and thermal effects in the rat brain under optogenetic stimulation. J. Biophoton. *9*, 576–585.

Han, X., Chow, B.Y., Zhou, H., Klapoetke, N.C., Chuong, A., Rajimehr, R., Yang, A., Baratta, M.V., Winkle, J., Desimone, R., et al. (2011). A high-light sensitivity optical neural silencer: development and application to optogenetic control of non-human primate cortex. Front. Syst. Neurosci. *5*, 18.

Huber, D., Petreanu, L., Ghitani, N., Ranade, S., Hromadka, T., Mainen, Z., and Svoboda, K. (2008). Sparse optical microstimulation in barrel cortex drives learned behaviour in freely moving mice. Nature *451*, 61–64.

Inoue, K., Del Carmen Marin, M., Tomida, S., Nakamura, R., Nakajima, Y., Olivucci, M., and Kandori, H. (2019). Red-shifting mutation of light-driven sodium-pump rhodopsin. Nat. Commun. *10*, 1993.

Johansson, J.D. (2010). Spectroscopic method for determination of the absorption coefficient in brain tissue. J. Biomed. Opt. *15*, 057005.

Kim, C.K., Adhikari, A., and Deisseroth, K. (2017). Integration of optogenetics with complementary methodologies in systems neuroscience. Nat. Rev. Neurosci. *18*, 222–235.

Klapoetke, N.C., Murata, Y., Kim, S.S., Pulver, S.R., Birdsey-Benson, A., Cho, Y.K., Morimoto, T.K., Chuong, A.S., Carpenter, E.J., Tian, Z., et al. (2014). Independent optical excitation of distinct neural populations. Nat. Methods *11*, 338–346.

Li, N., Chen, S., Guo, Z.V., Chen, H., Huo, Y., Inagaki, H.K., Chen, G., Davis, C., Hansel, D., Guo, C., et al. (2019). Spatiotemporal constraints on optogenetic inactivation in cortical circuits. eLife *8*, e48622.

Mahn, M., Gibor, L., Patil, P., Cohen-Kashi Malina, K., Oring, S., Printz, Y., Levy, R., Lampl, I., and Yizhar, O. (2018). High-efficiency optogenetic silencing with soma-targeted anion-conducting channelrhodopsins. Nat. Commun. *9*, 4125.

Maier, J.X., Blankenship, M.L., Li, J.X., and Katz, D.B. (2015). A multisensory network for olfactory processing. Curr. Biol. *25*, 2642–2650.

Mattis, J., Tye, K.M., Ferenczi, E.A., Ramakrishnan, C., O'Shea, D.J., Prakash, R., Gunaydin, L.A., Hyun, M., Fenno, L.E., Gradinaru, V., et al. (2011). Principles for applying optogenetic tools derived from direct comparative analysis of microbial opsins. Nat. Methods *9*, 159–172.

Miyamoto, K., Osada, T., Setsuie, R., Takeda, M., Tamura, K., Adachi, Y., and Miyashita, Y. (2017). Causal neural network of metamemory for retrospection in primates. Science *355*, 188–193.

Miyamoto, K., Setsuie, R., Osada, T., and Miyashita, Y. (2018). Reversible silencing of the frontopolar cortex selectively impairs metacognitive judgment on non-experience in primates. Neuron *97*, 980–989.e6.

Moreno-Garcia, A., Kun, A., Calero, O., Medina, M., and Calero, M. (2018). An overview of the role of lipofuscin in age-related neurodegeneration. Front. Neurosci. *12*, 464.

Ohayon, S., Grimaldi, P., Schweers, N., and Tsao, D.Y. (2013). Saccade modulation by optical and electrical stimulation in the macaque frontal eye field. J. Neurosci. *33*, 16684–16697.

Owen, S.F., Liu, M.H., and Kreitzer, A.C. (2019). Thermal constraints on in vivo optogenetic manipulations. Nat. Neurosci. *22*, 1061–1065.

Pisanello, F., Mandelbaum, G., Pisanello, M., Oldenburg, I.A., Sileo, L., Markowitz, J.E., Peterson, R.E., Della Patria, A., Haynes, T.M., Emara, M.S., et al. (2017). Dynamic illumination of spatially restricted or large brain volumes via a single tapered optical fiber. Nat. Neurosci. *20*, 1180–1188.

Robles, F.E., Chowdhury, S., and Wax, A. (2010). Assessing hemoglobin concentration using spectroscopic optical coherence tomography for feasibility of tissue diagnostics. Biomed. Opt. Express. *1*, 310–317.

Root, C.M., Denny, C.A., Hen, R., and Axel, R. (2014). The participation of cortical amygdala in innate, odour-driven behaviour. Nature *515*, 269–273.

Rungta, R.L., Osmanski, B.-F., Boido, D., Tanter, M., and Charpak, S. (2017). Light controls cerebral blood flow in naive animals. Nat. Commun. *8*, 14191.

Schmitt, J.M. (1986). Optical Measurement of Blood Oxygen by Implantable Telemetry (Stanford University).

Shin, Y., Yoo, M., Kim, H.S., Nam, S.K., Kim, H.I., Lee, S.K., Kim, S., and Kwon, H.S. (2016). Characterization of fiber-optic light delivery and light-induced temperature changes in a rodent brain for precise optogenetic neuromodulation. Biomed. Opt. Express. *7*, 4450–4471.

Sileo, L., Bitzenhofer, S.H., Spagnolo, B., Pöpplau, J.A., Holzhammer, T., Pisanello, M., Pisano, F., Bellistri, E., Maglie, E., De Vittorio, M., et al. (2018). Tapered fibers combined with a multi-electrode array for optogenetics in mouse medial prefrontal cortex. Front. Neurosci. *12*, 771.

Squire, L.R., Stark, C.E., and Clark, R.E. (2004). The medial temporal lobe. Annu. Rev. Neurosci. *27*, 279–306.

Stefanik, M.T., Kupchik, Y.M., Brown, R.M., and Kalivas, P.W. (2013). Optogenetic evidence that pallidal projections, not nigral projections, from the nucleus accumbens core are necessary for reinstating cocaine seeking. J. Neurosci. *33*, 13654–13662.

Stujenske, J.M., Spellman, T., and Gordon, J.A. (2015). Modeling the spatiotemporal dynamics of light and heat propagation for in vivo optogenetics. Cell Rep. *12*, 525–534.

Takatani, S., and Graham, M.D. (1979). Theoretical analysis of diffuse reflectance from a two-layer tissue model. IEEE Trans. Bio Med. Eng. *26*, 656–664.

Tamura, K., Ohashi, Y., Tsubota, T., Takeuchi, D., Hirabayashi, T., Yaguchi, M., Matsuyama, M., Sekine, T., and Miyashita, Y. (2012). A glass-coated tungsten microelectrode enclosing optical fibers for optogenetic exploration in primate deep brain structures. J. Neurosci. Methods *211*, 49–57.

Tamura, K., Takeda, M., Setsuie, R., Tsubota, T., Hirabayashi, T., Miyamoto, K., and Miyashita, Y. (2017). Conversion of object identity to object-general semantic value in the primate temporal cortex. Science *357*, 687–692.

Trouche, S., Perestenko, P.V., van de Ven, G.M., Bratley, C.T., McNamara, C.G., Campo-Urriza, N., Black, S.L., Reijmers, L.G., and Dupret, D. (2016). Recoding a cocaine-place memory engram to a neutral engram in the hippocampus. Nat. Neurosci. *19*, 564–567.

Tsubota, T., Okubo-Suzuki, R., Ohashi, Y., Tamura, K., Ogata, K., Yaguchi, M., Matsuyama, M., Inokuchi, K., and Miyashita, Y. (2015). Cofilin1

controls transcolumnar plasticity in dendritic spines in adult barrel cortex. PLoS Biol. *13*, e1002070.

Tsunematsu, T., Ueno, T., Tabuchi, S., Inutsuka, A., Tanaka, K.F., Hasuwa, H., Kilduff, T.S., Terao, A., and Yamanaka, A. (2014). Optogenetic manipulation of activity and temporally controlled cell-specific ablation reveal a role for MCH neurons in sleep/wake regulation. J. Neurosci. *34*, 6896–6909.

Tye, K.M. (2011). Amygdala circuitry mediating reversible and bidirectional control of anxiety. Nature *471*, 358–362.

Tye, K.M., and Deisseroth, K. (2012). Optogenetic investigation of neural circuits underlying brain disease in animal models. Nat. Rev. Neurosci. *13*, 251–266.

Vo-Dinh T, E. (2003). Biomedical Photonics Handbook (CRC Press).

Wenker, I.C., Abe, C., Viar, K.E., Stornetta, D.S., Stornetta, R.L., and Guyenet, P.G. (2017). Blood pressure regulation by the rostral ventrolateral medulla in conscious rats: effects of hypoxia, hypercapnia, baroreceptor denervation, and anesthesia. J. Neurosci. *37*, 4565–4583.

Wiegert, J.S., Mahn, M., Prigge, M., Printz, Y., and Yizhar, O. (2017). Silencing neurons: tools, applications, and experimental constraints. Neuron *95*, 504–529.

Xu, C., Krabbe, S., Grundemann, J., Botta, P., Fadok, J.P., Osakada, F., Saur, D., Grewe, B.F., Schnitzer, M.J., Callaway, E.M., et al. (2016). Distinct hippocampal pathways mediate dissociable roles of context in memory retrieval. Cell *167*, 961–972.e16.

Yaroslavsky, A.N. (2002). Optical properties of selected native and coagulated human brain tissues in vitro in the visible and near infrared spectral range. Phys. Med. Biol. *47*, 2059–2073.

Yizhar, O., Fenno, L.E., Davidson, T.J., Mogri, M., and Deisseroth, K. (2011). Optogenetics in neural systems. Neuron *71*, 9–34.

Zijlstra, W.G., Buursma, A., Falke, H.E., and Catsburg, J.F. (1994). Spectrophotometry of hemoglobin: absorption spectra of rat oxyhemoglobin, deoxyhemoglobin, carboxyhemoglobin, and methemoglobin. Comp. Biochem. Physiol. B Comp. Biochem. *107*, 161–166.

iScience, Volume *23*

Supplemental Information

Off-Peak 594-nm Light Surpasses On-Peak 532-nm Light in Silencing Distant ArchT-Expressing Neurons In Vivo

Rieko Setsuie, Keita Tamura, Kentaro Miyamoto, Takamitsu Watanabe, Masaki Takeda, and Yasushi Miyashita

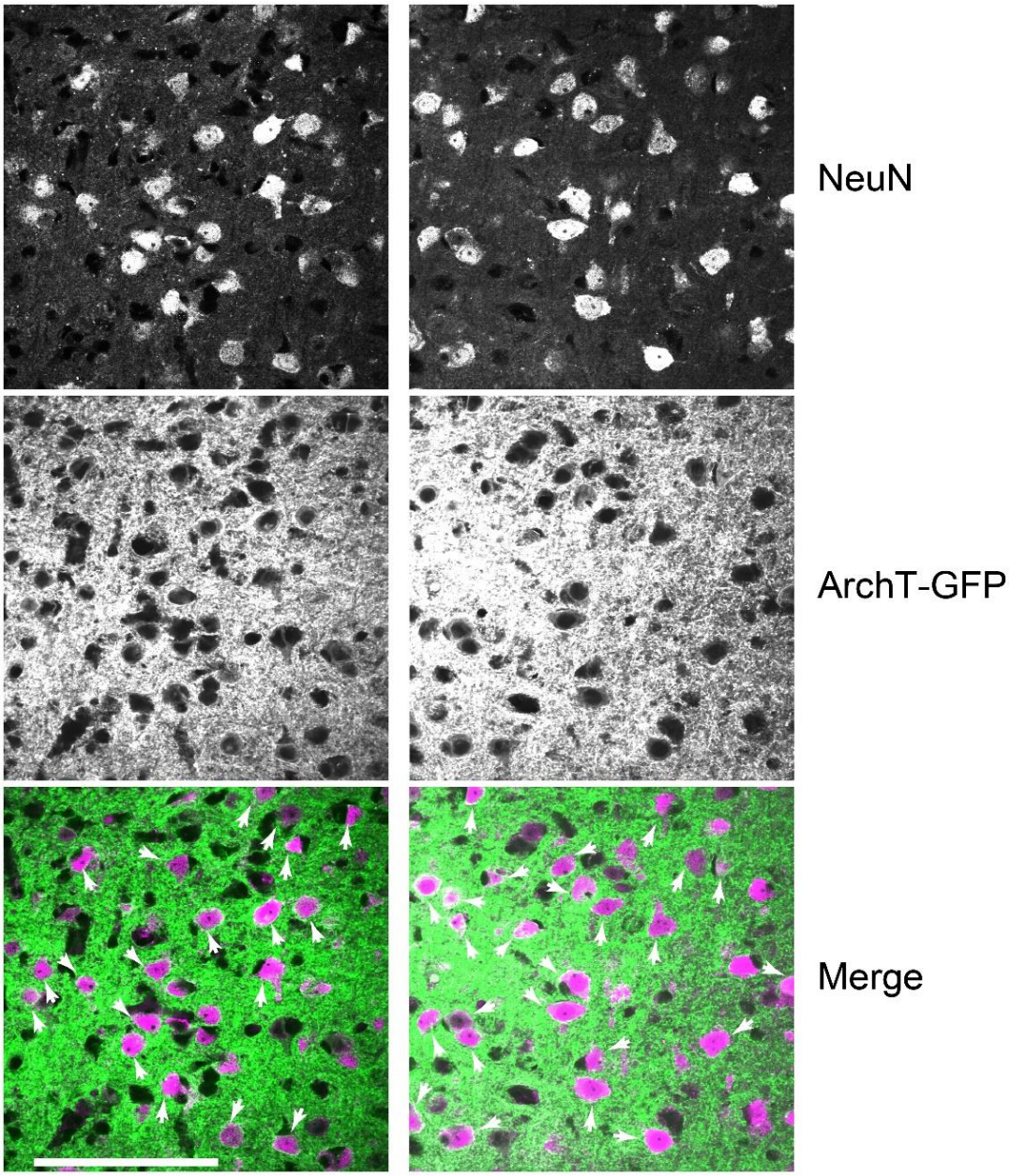

Figure S1.

ArchT-GFP expression in the rat cortex, Related to Figure 1.

Confocal images of the ArchT expression area in Figure 1C. Top: Grayscale image for NeuN, Middle: Grayscale image for ArchT-GFP, Bottom: colored merged image for NeuN (magenta) and ArchT-GFP (green). The scale bar indicates 200 μm. The white arrows indicate ArchT-GFP-expressing neurons.

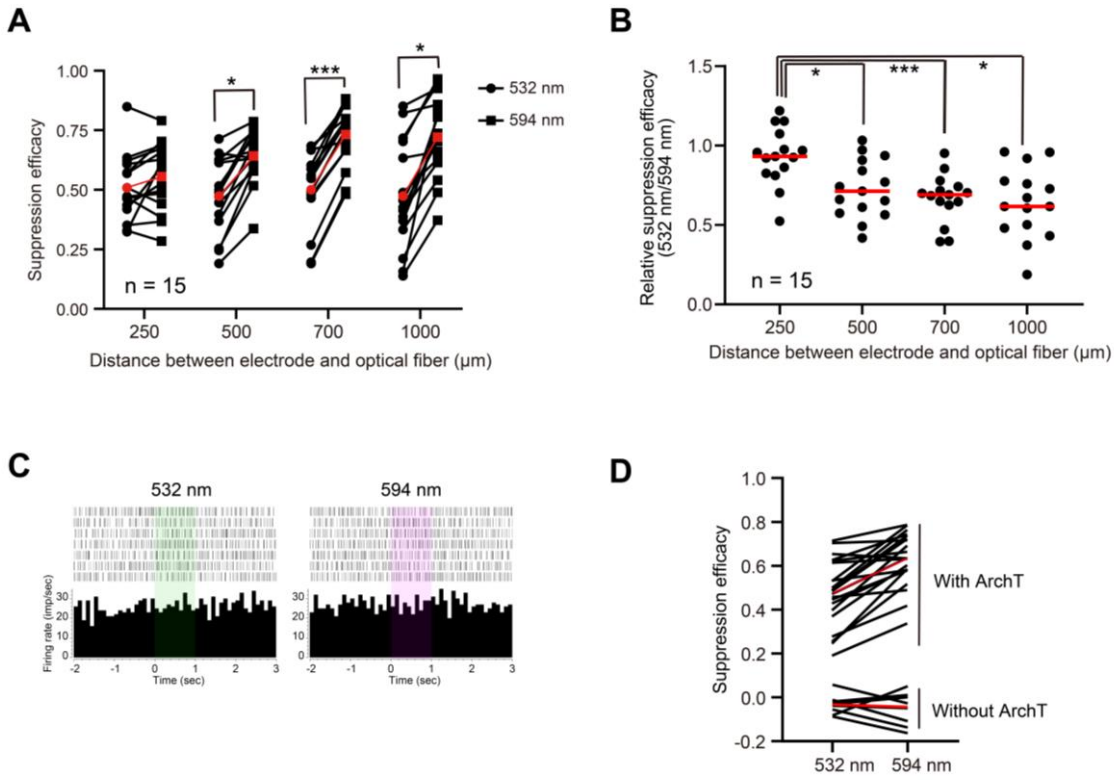

Figure S2.

Comparison of the suppression efficacy between 532 nm and 594 nm light at four different distances using data that include those outside the dynamic range (A and B), and the effect of photoillumination on non-ArchT expressing neurons in naïve rat (C and D), Related to Figure 3.

A, Suppression efficacy of 532 nm (circle) and 594 nm (square) light at different distances. The black lines indicate individual units and the red lines indicate the mean of the units [two-way ANOVA: main effect of wavelength, $F(1, 28) = 15.35$, $p = 0.0005$; main effect of distance, $F(3, 84) = 3.029$, $p = 0.034$; interaction between distance and wavelength, $F(3, 84) = 4.29$, $p = 0.0073$; Bonferroni's multiple comparison: $p > 0.999$, $p = 0.018$, $p = 0.0005$, $p = 0.002$ for 250, 500, 700, and 1,000 μm respectively]. **B**, Relative suppression efficacy between 532 nm and 594 nm light at different distances. The circles indicate individual units and the red lines indicate the mean of the units [one-way ANOVA: main effect of distance, $F(3, 42) = 7.54$, $p = 0.0004$; followed by Tukey's multiple comparison: $p = 0.021$ (250 μm vs 500 μm), $p = 0.0019$ (250 μm vs 700 μm), and $p = 0.0006$ (250 μm vs 1,000 μm)]. **C,** Raster and PSTH of a representative single-unit illuminated with the light power of 5 mW (the highest light power used at a distance of 500 μm in the experiment depicted in Figure 3) with either 532 nm light (left) or 594 nm light (right) at the distance of 500 μm with naïve rat. The shaded area demarcates the stimulation period with 1-s continuous light illumination. Bin size is 100 ms. **D,** The population analysis of the single-unit, plotted on the same graph as in Figure 3C at 500 μm, illuminated with either 532 nm or 594 nm light in naïve rat. The black lines indicate individual units, and the red lines indicate the mean of the units [$p = 0.725$ ($n=8$), paired t-test].

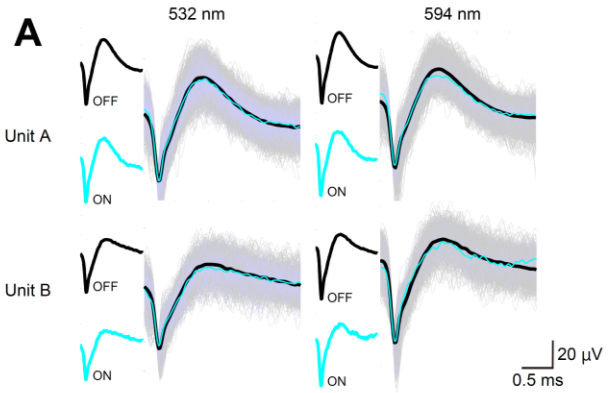
A
532 nm
594 nm
Unit A
Unit B
OFF
ON
20 μV
0.5 ms

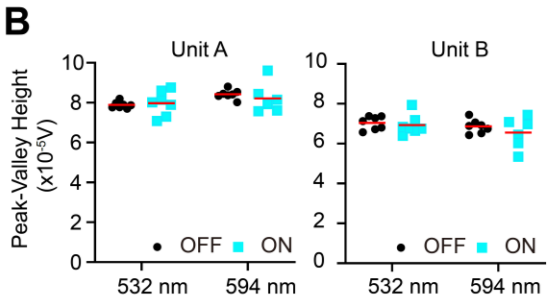
B
Unit A
Unit B
Peak-Valley Height (x10⁻⁵V)
OFF
ON
532 nm
594 nm

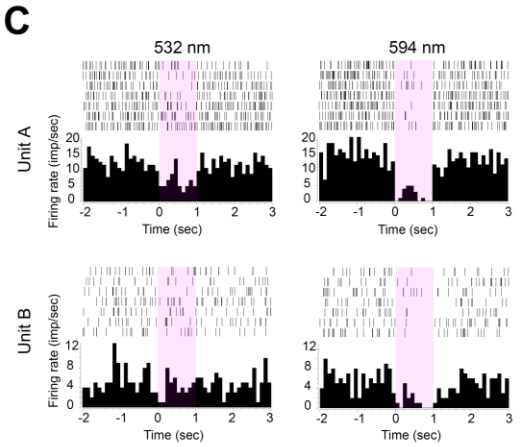
C
532 nm
594 nm
Unit A
Unit B
Firing rate (imp/sec)
Time (sec)

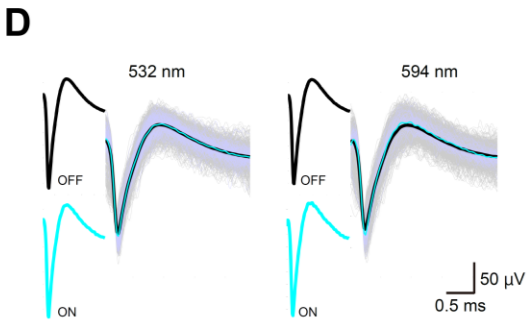
D
532 nm
594 nm
OFF
ON
50 μV
0.5 ms

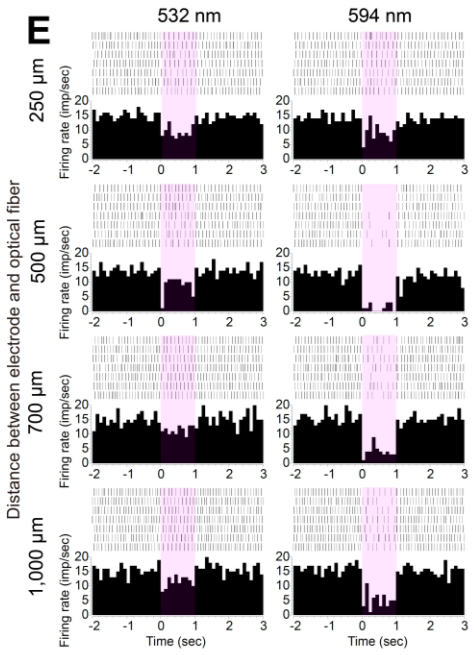
E
532 nm
594 nm
Distance between electrode and optical fiber
250 μm
500 μm
700 μm
1,000 μm
Firing rate (imp/sec)
Time (sec)

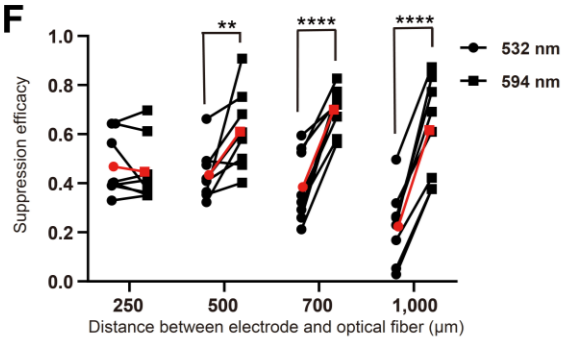
F
Suppression efficacy
532 nm
594 nm
Distance between electrode and optical fiber (μm)

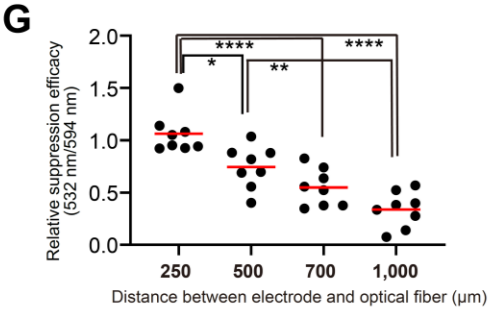
G
Relative suppression efficacy (532 nm/594 nm)
Distance between electrode and optical fiber (μm)

Figure S3.

Comparison of the suppression efficacy between 532 nm and 594 nm light at four different distances using only the single-unit data, Related to Figure 3.

A-C Analysis of two single-units sorted offline from the representative multi-unit (at the distance of 1,000 μm), whose data are depicted in Figure 3B. **A.** Spike waveforms of the two single-units (Unit A in the upper panel, and Unit B in the lower panel) with either 532 nm (left) or 594 nm (right) photostimulation. Gray and pale-blue traces indicate the waveforms of the spikes (large panel), and black (small upper panel and large panel) and light-blue traces (small lower panel and large panel) indicate the means of these waveforms, without and with photostimulation, respectively. **B.** Peak-valley height of spikes without (black circles) and with (light-blue squares) photostimulation. Each circle/square represents a mean peak-valley height of spikes detected 1-s before and 1-s during photostimulation in a train (n = 7 trains in a trial; since one train of photostimulation period did not include any spikes with 594-nm light for both Unit A and Unit B (See raster plot in Figure S3C), the number of light-blue squares is 6) [two-way ANOVA: for Unit A; main effect of light, $F(1, 6) = 0.097$, $p = 0.77$; main effect of wavelength, $F(1, 6) = 4.81$, $p= 0.071$; interaction between wavelength and light, $F(1, 5) = 1.04$, $p = 0.36$: for Unit B; main effect of light, $F(1, 6) = 1.51$, $p = 0.26$; main effect of wavelength, $F(1, 6) = 2.67$, $p = 0.26$; interaction between wavelength and distance, $F(1, 5) = 1.16$, $p = 0.33$]. **C** Raster and PSHT of Unit A (upper) and Unit B (lower) with either 532 nm light (left) or 594 nm light (right) photostimulation. The shaded area demarcates the stimulation period with 1-s continuous light illumination. Bin size is 100 ms. **D-E,** Analysis of another offline sorted single-unit. **D**, Spike waveforms as in A (the spike waveforms from the unit at the distance of 1,000 μm depicted in Figure S3E). **E**, Raster and PSHT of the single-unit with either 532 nm light (left) or 594 nm light (right) photostimulation at four different distances. The shaded area demarcates the stimulation period with 1-s continuous light illumination. Bin size is 100 ms. **F-G**, Population analysis of the offline sorted single-units. **F,** Suppression efficacy of 532 nm (circle) and 594 nm (square) light at four different distances. The black lines indicate individual units and the red lines indicate the mean of the units [two way ANOVA; main effect of distance, $F(3, 21) = 4.375$, $p=0.153$; main effect of wavelength, $F(1,7) = 71.09$, $p < 0.0001$; interaction between distance and wavelength, $F(3, 21) = 17.44$, $p <0.0001$; followed by Bonferroni's multiple comparisons, $p > 0.999$, $p = 0.0023$, $p < 0.0001$, $p < 0.0001$ for 250, 500, 700, and 1,000 μm respectively]. **G**, Relative suppression efficacy between 532 nm and 594 nm light at four different distances. The relative suppression efficacy for each unit is the ratio (532 nm/594 nm) of the suppression efficacy between 532 nm and 594 nm light at each distance. The black circles indicate individual units, and the red lines indicate the mean of the units. [one-way ANOVA; $F(3, 21) = 22.72$, $p < 0.0001$; followed by Tukey-Kramer's multiple comparisons, $p = 0.011$ (250 μm vs 500 μm), $p < 0.0001$ (250 μm vs 700 μm, and 250 μm vs 1,000 μm), $p = 0.0012$ (500 μm vs 1,000 μm) respectively] * $p < 0.05$, ** $p < 0.01$, **** $p < 0.0001$

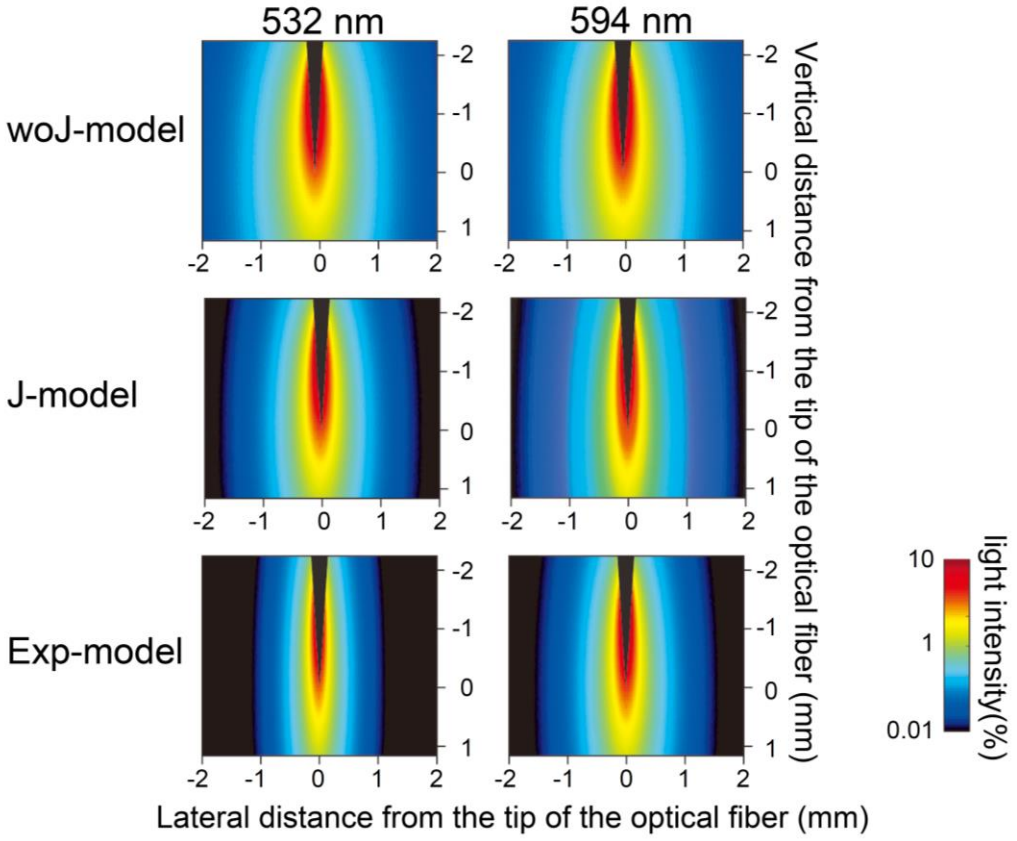

Figure S4.

Estimation of light propagation with Monte Carlo simulation, Related to Figure 4.

2D light intensity patterns that result from Monte Carlo simulations for the woJ-model (top), J-model (middle), and Exp-model (bottom), each with 532 nm (left) and 594 nm (right) light with color-coding on a log scale (see Transparent Methods 'Monte Carlo simulation' for details). For J-model simulation, a set of parameters ($\mu_a(\lambda)$, $\mu_s(\lambda)$ and $\mu_{af}(\lambda)$) obtained experimentally in vivo by Johansson (Johansson, 2010) were applied. For woJ-model simulation, $\mu_a(\lambda)$ was set to 0, along with the same $\mu_s(\lambda)$ and $\mu_{af}(\lambda)$ as those in J-model. For Exp-model simulation, $\mu_a(\lambda)$ was estimated to fit the light propagation patterns obtained from the Exp-data (light) [$^{Exp}\mu_a(\lambda)$; see Transparent Methods 'Estimation of the absorption coefficients for Exp-data (light)' for details] along with the same $\mu_s(\lambda)$ and $\mu_{af}(\lambda)$ as those in J-model.

Note that Figure 4B is plotted with normalized input light power calculated from the number of photons observed at the lateral distances of 0, 250, 500, 700, and 1,000 μm from the tip of the side-emitting optical fiber. Precisely, the number of photons, obtained from the simulation, was converted to light power [2330.5 meV/photon for 532 nm light and 2087.3 meV/photon for 594 nm light (Hesse et al., 2007)], which was adjusted to equalize the light power at 0 μm of both light wavelengths within the same model. Then, the relative input light power to deliver equal light power at each distance for both 532 nm and 594 nm was calculated and normalized by the input light power for 532 nm at 250 μm in the same model.

Transparent Methods

Animals and ethics statements

All animal procedures were conducted under a protocol approved by the University of Tokyo Animal Care Committee (permit number, MED: P16-072), which complied with the National Institutes of Health (NIH; Bethesda, MD, USA) Guide for the Care and Use of Laboratory Animals. All surgical procedures were performed under anesthesia, and all efforts were made to minimize the suffering and number of animals employed. Thirty-four male Wister rats (Nihon SLC, Japan) were used in this study.

Injection of a viral vector to the rat cortex

Male Wister rats between the age of 10 and 15 weeks were injected with a viral vector. Briefly, the rats were anesthetized with isoflurane (~3% for induction and ~1% for maintenance) by using an anesthetizer (MK-AT200D; Muromachi Kikai, Tokyo, Japan). They were fixed in a stereotaxic apparatus (SR-6R; Narishige, Tokyo, Japan). A small hole was drilled in the skull over the somatosensory area (3.0 mm posterior to bregma, and 2.9 mm lateral to the midline) under a microscope (MA80; Leica, Wetzlar, Germany). A glass pipette (~50 μm tip-diameter), which was attached to a 10-μl Hamilton syringe (Hamilton Company, Reno, NV, USA), was vertically inserted into the cortex to a depth of 0.9 – 1.0 mm below the dura mater. The viral vector encoding ArchT fused to a green fluorescent protein (ArchT-GFP) under the Ca^{2+}/calmodulin-dependent protein kinase II (CaMKII) promoter (AAV5-CaMKIIa-ArchT-GFP; titer, 10^{10} GC/ml; volume, 2 μl/site/rat; purchased from University of Pennsylvania Vector Core, Philadelphia, PA, USA) was injected at a flow rate of 200 nl/min using a micropump system (UltramicroPump III and Micro4; World Precision Instruments, Sarasota, FL, USA). The pipette was left in place for 10 min before and 20 min after the injection. The scalp incision was carefully sutured, and the rat was returned to its home cage after recovering from anesthesia (Tsubota et al., 2015).

Immunofluorescent analysis of ArchT-GFP expression in the rat cortex

Five to 8 weeks after the virus injection, five rats, which included three rats after the optogenetic experiments, were sacrificed by sodium pentobarbital (90 mg/kg; i.p.) and perfused transcardially with saline followed by 4% paraformaldehyde (PFA) in phosphate-buffered saline (PBS) (Matsuyama et al., 2015). The extracted brain was post-fixed in 4% PFA overnight, cryoprotected in 30% wt/vol sucrose in PBS at 4 °C, and finally embedded in OCT compound (Sakura, Tokyo, Japan) on dry ice. The brain was cut into 20 μm coronal sections using a cryostat (CM3050S, Leica, Wetzlar, Germany). Slices were subjected to immunofluorescence analysis (Setsuie et al., 2007; Tamura et al., 2017). In brief, the sections were incubated in a blocking solution of 5% normal goat serum (NGS; Vector Laboratories, Burlingame, CA, USA) and 0.3% Triton X-100 in phosphate-buffered saline for 1 hr at room temperature. Samples were subsequently incubated with the primary antibodies at 4 °C overnight with primary antibodies [rabbit anti-GFP antibodies (1:2,000; MBL International, Woburn, MA, USA) and mouse anti-NeuN antibodies (1:1,000; Merck Millipore, Darmstadt, Germany)], followed by a 1-hr incubation with the secondary antibodies at room temperature [AlexaFluor488-conjugated goat anti-rabbit IgG antibodies (1:1,000; Invitrogen The Thermo Fischer Scientific, Waltham, MA, USA) and AlexaFluor561-conjugated goat anti-mouse IgG antibodies (1:1,000; Invitrogen)]. Fluorescence images were obtained using a

fluorescence microscope (BZ-9000; Keyence, Osaka, Japan) and a confocal laser scanning microscope (FV3000RS; Olympus, Tokyo, Japan).

To determine the percentage of ArchT-expressing neurons, we counted more than a hundred NeuN positive cells in each of the two ArchT-expressing rats (rat 1, n = 114; rat 2, n = 156), and identified that an average of 71% of these neurons (rat 1, 77%; rat 2, 65%) was ArchT positive.

Fabrication of the electro-fiberoptic array

We fabricated an electro-fiberoptic array that contained a microelectrode and four side-emitting optical fibers horizontally placed at defined distances. The electro-fiberoptic array was first put together, and the tip of the array was then immersed as a whole in a glass-etching solution to yield the side-emitting property of the optical fibers.

A large core, step-index multimode silica fiber was selected for our electro-fiberoptic array (core, 105 μm; clad, 125 μm; numerical aperture, 0.22; FG105UCA, Thorlabs, NJ, USA). Optical fibers were pulled to create a tapered tip by using a micropipette puller installed with a micro gas torch (Tamura et al., 2012). Under the microscope, four tapered optical fibers and one tungsten microelectrode (WE30030.5A5; Microprobes, MD, USA) were inserted into a 24-hole ferrule of an MT optical fiber connector (hole arrangement, 2 × 12; hole diameter, 125 μm; hole spacing, 500 μm × 250 μm; 24 MT-PF-M, Hakusan-MFG, Kanazawa, Japan). Each optical fiber was intended to be arranged at the horizontal distances of 250, 500, 700, and 1,000 μm from the microelectrode (Figure 3A). The tips of the four optical fibers were carefully aligned at the same depth, and the tip of the microelectrode was placed slightly (~300 μm) shallower from the tips of the optical fibers. This array was then firmly fixed with a light-curable adhesive (Loctite 4304, Henkel, Düsseldorf, Germany).

The side-emitting surface of the optical fibers was created by soaking the tip of the entire electro-fiberoptic array (up to ~6 mm from the tip, full length from the MT connector surface) in a hydrofluoric-acid-free nontoxic glass etching solution (prewarmed at 42 °C; reaction time, 8 minutes; QE-CL2N, Frostec, Fukuoka, Japan) by using a micromanipulator under a stereomicroscope. The array was then immersed and gently shaken in an excess amount of water to halt the glass etching reaction and to prevent the subsequent recrystallization of the melted debris.

Analysis of the light emission properties of the side-emitting optical fibers

To evaluate the side-emitting properties of our optical fibers, the emission of 473 nm light from the side-emitting optical fiber (n = 6 independent fibers) was observed and imaged in a 10 nM fluorescein solution under a fluorescence microscope (VB-G05; Keyence) through a yellow fluorescent protein (YFP) filter (Keyence BZ) (Figure 1B). The light input power was optimized to avoid saturation of the images. For comparison, the light emission from conventional blunt-end optical fibers (graded-index multimode fiber; GIF50C, Thorlabs) without tapering and etching was also observed and imaged (n = 6). Image data were analyzed using Image J software (NIH, Bethesda, MD, USA). Pixel values in the lateral and axial directions were normalized to the maximum value (= 100) at the tip of each optical fiber (Figure 1B).

Electrophysiological recording and optogenetic stimulation

Four to 8 weeks after the injection of the virus vector, each rat was anesthetized with isoflurane (~3% for induction and ~1% for maintenance) and was fixed in a stereotaxic apparatus (SR-6R; Narishige) (Tsubota et al., 2015). Body temperature was maintained at approximately 37 °C throughout the experiment by using a heating pad (Nihon Bioresearch, Nagoya, Japan). The skull and dura over the somatosensory area were removed to expose the cortex. After the craniotomy and durotomy, anesthesia was switched to ethyl carbamate (1.2 g/kg body weight, i.p.). The in vivo GFP fluorescence derived from ArchT-GFP expression was verified under a fluorescence microscope (VB-G05; Keyence) installed with a CCD camera (VB-7000; Keyence). The electro-fiberoptic array was slowly inserted into the cortex by using a hydraulic micromanipulator (MO-10, Narishige) under a stereomicroscope (MO80, Leica).

For the unit recording, the electrical signal was amplified (2×10^4) and band-pass filtered (50-10 kHz, Nihon Koden, Tokyo, Japan), and then monitored online and stored by using Recorder software (Neural Data Acquisition System, Plexon, TX, USA) (Tamura et al., 2012). We recorded both single- and multi-units online by voltage trigger at a certain threshold, and then a time-voltage window filtering for spike waveforms with a time-voltage window discriminator (Time-Amplitude Window Discriminator, EN-611J: Nihon Kohden). When the filtered unit contained multiple distinct waveforms, we defined the unit as a multi-unit, and when the filtered unit contained similar waveforms, we defined the unit as a single-unit.

For photostimulation, a 532 nm (Opus532-6000MPC; Laser Quantum, Stockport, UK) or a 594 nm (FKL594.100.CWA.L; Cobolt AB, Solna, Sweden) diode-pumped solid-state laser was used as the light source. Each laser beam entered into a relay optical fiber through a circular neutral density (ND) filter (NDC-25C-2/4; Thorlabs) and an electrically controlled mechanical shutter (Model LS2T2; Uniblitz, Rochester, NY, USA). Light power was modulated by the ND filter, whose filtering percentage was remotely controlled by the software (Thorlabs). The timing of light delivery was managed with a mechanical shutter.

In the experiment to determine the relationship between light power and suppression efficacy for 532 nm and 594 nm light (Figure 2), we first determined the emitting light power necessary to suppress approximately 60% of the unit's firing ($P_{0.6}$). The units were recorded only when the neuronal activity of the unit could be completely suppressed by a brief preliminary qualitative testing. The light was emitted at six levels or more of light power, which were determined by $P_{0.6}$, ranging from minimum suppression (0%) to maximum suppression (100% or less), in a randomized order. For each light power, 1-s light was delivered seven times in a 20-s interval (Figure 2A). A total of 9 (2 single and 7 multi) units and 6 (1 single and 5 multi) units were recorded for 594 nm and for 532 nm light, respectively. Note that the units used for either 532 nm or 594 nm light illumination in the experiment for Figure 2 were independent.

In the experiment to examine the effect of light wavelength and distance on neural suppression in each unit (Figure 3), eight conditions in total (two wavelengths delivered at four distances) were tested for the same unit (Figure 3A). The units were recorded only when the neuronal activity of the unit could be completely suppressed by a brief preliminary qualitative testing. These eight conditions were switched by connecting the 532 nm relay fiber or the 594 nm relay fiber to any of the four optical fibers (which were installed at a distance of 250, 500, 700, and 1,000μm) within the array. For each condition, 1-s light was delivered seven times in a 20-s interval.

The photostimulations with 532 nm and 594 nm light at the same distance were always paired and run consecutively with the no-photostimulation baselines in between. The four pairs of recordings (532 nm and 594 nm) with photostimulation from four different distances were randomized (Figure 3A) within a block of recording. The light power was adjusted according to the photostimulation distance so that the comparison was conducted within the dynamic range of neuronal firing (determined from Figure 2) as follows.

In brief, we determined the emitting light power of 594 nm light at the distance of 500 μm ($P_{0.6/500}$) necessary to suppress approximately 60% of the unit's firing. $P_{0.6/500}$ was scaled to take into account the light's inverse squared decay over distance to determine the emitting light power at the distances of 250, 700, and 1,000 μm with 594 nm light. The same emitting light power as 594 nm light was always emitted with 532 nm light at each distance.

The preliminary experiment confirmed that the emitting light power determined by this protocol suppressed the neuronal firing within the dynamic range, at all four distances, without causing a suppression effect that was too weak (i.e., flooring effect) or too strong (i.e., ceiling effect), in most instances. We did not try to exactly match the emitted light from each fiber to the scaled value with decay over the distance (see input value in Figure 3B). In contrast, we paid special care to ensure that the emitting light power matched precisely between the two wavelengths at the same distance by the following procedure.

We calibrated the quantitative relationship between the different levels of input light power from the 532 nm relay fiber or the 594 nm relay fiber, and the corresponding emitting light power from the tip of each of the four optical fibers (installed at the distance of 250, 500, 700, 1,000 μm) within the electro-fiberoptic array, by measuring the light powers by a power meter taking the wavelength into account (PM100D, Thorlabs). This calibration was conducted before inserting the electro-fiberoptic array into the cortex in each experiment, which enabled the accurate control of light power emitted from each optical fiber.

The power emitted from the optical fiber was set below 15 mW to avoid the heat-induced activation of neurons and damage to the tissue by continuous illumination (Owen et al., 2019; Stujenske et al., 2015). As we have already described above, the emitting light power for the distances other than 500 μm was mathematically determined by taking into account the presumed light's inverse squared decay over distance, based on the experimentally determined laser power for 500 μm, for the experiments for Figure 3,. Thus, the suppression efficacy at some distance reached the plateau range on occasion. As we defined 81% as an upper limit of suppression efficacy within the dynamic range (Figure 2G), the data outside this dynamic range in which more than 81% of units' firing was suppressed in response to photostimulation, were excluded from the analysis (Figure 3C and 3D; see below for the reasons of excluding the data). The data with the unstable basic firing rate during the no-illumination period were also excluded from the analysis (Figure 3C and 3D). In both cases, the corresponding data of the other wavelength at the same distance in the unit were also excluded (that is, if the data at 1,000 μm with 594 nm reached the plateau range, then the data at 1,000 μm with 532 nm was excluded as well). The number of units included in the analysis for Figure 3C and 3D is as follows: 16 (4 single and 12 multi) units, 21 (5 single and 16 multi) units, 15 (3 single and 12 multi) units, and 16 (4 single and 12 multi) units for 250, 500, 700, 1,000 μm respectively.

As we have already explained above, we used different units for each of 532 nm and 594 nm light

conditions for the experiment in Figure 2. The different levels of ArchT expression in each unit and the different types of neurons that express ArchT is likely to be a cause of variability for the EP50 values across units, and consequently, leading to a different average between light wavelength conditions (see the $\beta_{inflection}$ values for 532 nm and 594 nm in the result section). Similar variabilities of light intensities to suppress the neurons in vivo have also been reported (Mahn et al., 2018), with GtACR, inhibitory anion-conducting channelrhodopsin. In order to eliminate the effect of the difference in light responsiveness between the units, and to directly compare the suppression efficacies between two wavelengths of light with accuracy, we measured the suppression efficacy of the eight conditions [2 wavelengths (532 nm and 594 nm) × 4 distances (250, 500, 700, and 1,000 μm)] from the same unit in each experiment session in Figure 3.

Sorting and analysis of single unit

For the analysis of single-units, we sorted the single-units offline from our raw continuous data using Offline sorter software (Plexon Inc, Texas, USA). We performed the analysis of spike waveforms and the peak-valley height with MATLAB software (The MathWorks Inc, MA, USA).

Optogenetic data analysis

We defined the suppression efficacy (supEff) of neuronal activity in response to illumination by using the firing rate (FR), as depicted below:

$$\text{supEff} = 1 - \frac{\text{mean(FR[1s during the illumination])}}{\text{mean(FR[1s before the illumination])}}$$

The relative suppression efficacy was defined as the ratio of the supEff of 532 nm light to the supEff of 594 nm light. To quantify the relationship between light power (Pw) and supEff for ArchT-expressing neurons, we obtained the power-suppression curve at 500 μm by fitting the suppression efficacy values measured at different light powers by using logistic regression:

$$\text{supEff(Pw = x)} = \beta_{\text{supEffmax}} - \frac{\beta_{\text{supEffmax}}}{1 + \left(\frac{x}{\beta_{inflection}}\right)^{\beta_{steepness}}}$$

in which supEff (Pw=x) represents supEff when the light power is x. The coefficients of the logistic model ($\beta_{supEffmax}$, $\beta_{inflection}$, $\beta_{steepness}$) capture the maximum plateau (corresponding to maximum supEff), the inflection point (corresponding to the light power required for half-maximum suppression), and the steepness of the curve (corresponding to the Hill's slope value), respectively. The range of $\beta_{supEffmax}$ is restricted ≤ 1, and thus, the suppression efficacy of EP50 is not 50% by definition.

This logistic fitting was conducted for each unit. We defined $\beta_{inflection}$ as the half-maximum effective light power EP50 (note that maximum suppression ($\beta_{supEffmax}$) is not necessarily 1 depending on the individual units). For the population analysis, the light power value of EP50 was normalized as 1 in each unit. Then the coefficients to fit all units' data points were estimated for both 594 nm light and 532 nm light. The slope at normalized EP50 in each unit was estimated by obtaining the first derivative of the fitted curve. The estimated coefficients of this logistic regression for each unit and those for all units after the normalization of the light power are summarized and compared between the 532 nm and 594 nm lights in the result section.

To compare how much emitting light power would be required to deliver half-maximum ArchT-mediated suppression by two wavelengths and four different distances (Figure 4A), we estimated these emitting light power by using power-suppression curves (Figure 2D and 2E), and by measuring supEff with changing distances/wavelength (Figure 3) as follows.

First, by projecting supEff value of each data point in Figure 3 onto the population power-suppression curves (magenta curve in Figure 2D, or green curve in Figure 2E), the corresponding light power was defined as the normalized light power (Pw_{norm}) for that data point. Second, the actual light power emitted from the optical fiber in each experiment was multiplied by $1/Pw_{norm}$. The obtained value would be the estimated emitting light power that is required to deliver half-maximum suppression (estEP50) in each condition. The estEP50 (mW) for 532 nm light was 0.75 ± 0.14, 4.18 ± 0.99, 7.15 ± 1.04, 22.88 ± 5.47 (mean ± SEM) for 250, 500, 700, and 1,000 μm respectively. The estEP50 (mW) for 594 nm light were 0.75 ± 0.143, 2.49 ± 0.55, 4.13 ± 0.44, 9.11 ± 1.08 (mean ± SEM) for 250, 500, 700, and 1,000 μm respectively. Finally, the estEP50 was normalized to the mean estEP50 for 532 nm photostimulation at a distance of 250 μm and plotted as relative input light power for equal suppression in Figure 4A.

The EP50 of ArchT is reported as ≈7 mW/mm^2 with 532 nm light for cultured hippocampal neurons expressing ArchT (Mattis et al., 2011). The mean estEP50 at the distance of 250 μm is 0.75 ± 0.14 mW (mean ± SEM) for 532 nm light. Assuming that the light illumination density of the emitted surface of our side-emitting optical fiber is uniform, the estEP50 would be 4.82 ± 0.90 mW/mm^2 (mean ± SEM). Thus, the estEP50 obtained from our experiment is in a similar order of magnitude.

As already described above, for the experiment in Figure 3, the light power emitted from the optical fiber was set below 15 mW to avoid the heat-induced activation of neurons and damage to the tissue by continuous illumination (Owen et al., 2019; Stujenske et al., 2015). Mean estEP50 at 1,000 μm is 22.88 ± 5.47 (mean ± SEM) for 532 nm light, which is over 15 mW but is 9.11 ± 1.08 (mean ± SEM) for 594 nm light. From Figure 4A, the distance at which the estEP50 is 15 mW for 594 nm light, is roughly around 1,200 μm.

Monte Carlo simulation

We conducted a random-walk Monte Carlo simulation of photon packets through three-dimensional space in the brain. For this purpose, we first used a script of Zemax OpticStudio (Zemax LLC), which was kindly shared by Dr. Pisanello (Pisanello et al., 2017; Sileo et al., 2018) and simulated traces of the photons inside the side-emitting fiber. Then, based on a script of MATLAB (The MathWorks Inc, MA, USA) originally developed by Dr. Stujenske and his colleagues (Stujenske et al., 2015), we simulated how the light propagated outside of the fiber. The simulation requires a set of 3 input parameters: scattering coefficients $\mu_s(\lambda)$ (λ = wavelength), absorption coefficients $\mu_a(\lambda)$, and anisotropy factor $\mu_{af}(\lambda)$. We simulated light propagations by using the following three sets of parameters.

The first set of parameters (J-model) was obtained experimentally in vivo by Johansson (Johansson, 2010). We extracted ${}^{J}\mu_a(\lambda)$ for either 532 nm or 594 nm light from a graph curve of the total ${}^{J}\mu_a(\lambda)$ in Figure 6 of the study (Johansson, 2010; ${}^{J}\mu_a(532) = 0.254\ mm^{-1}$, ${}^{J}\mu_a(594) = 0.145\ mm^{-1}$). We extracted ${}^{J}\mu_s(\lambda)$ and ${}^{J}\mu_{af}(\lambda)$ by linear interpolation from the measured values in the gray matter for the different wavelengths listed in Table 1 of

the same work (Johansson, 2010; $^{J}\mu_s(532)$ = 10.155 mm^{-1}, $^{J}\mu_s(594)$ = 8.510 mm^{-1}, $^{J}\mu_{af}(532) = {}^{J}\mu_{af}(594)$ = 0.89 mm^{-1}). It should be noted that the Johansson's absorption coefficients do not reflect the effect of the light absorption by oxy-hemoglobin (Figure Legend for Fig6; Johansson, 2010). In addition, the coefficients may only partially represent the absorption effects by the deoxy-hemoglobin because the blood content was lower than normally expected (Discussion on page 057005-6; Johansson, 2010).

In the second set of parameters (woJ-model), $\mu_a(\lambda)$ was set to 0, along with the same $\mu_s(\lambda)$ and $\mu_{af}(\lambda)$ as those in J-model. Note that the original MATLAB script developed by Dr. Stujenske and colleagues (Stujenske et al., 2015) does not allow direct simulation of how the light propagates when the outside-fiber environment has a zero-absorption coefficient. Therefore, we estimated light propagation in zero-absorption conditions using linear extrapolation in the vicinity of the zero-absorption coefficient. Specifically, we first repeated the light propagation simulation for small absorption coefficients ranging from 0.005 to 0.1 mm^{-1} by intervals of 0.005. Then, using the resultant light intensity maps, we linearly extrapolated the light intensity in zero-absorption conditions for each pixel. In this woJ-model, we simulated the light propagation by considering only the spatially non-homogeneous light scattering in the brain tissue.

In the third set of parameters (Exp-model), $^{Exp}\mu_a(\lambda)$ was estimated by the light propagation patterns obtained from the experimental data [Exp-data (light)] for the lateral direction (see below for details), along with the same $\mu_s(\lambda)$ and $\mu_{af}(\lambda)$ as those in J-model.

Based on the results of these simulations (Figure S4), we calculated the relative input light power required to deliver equal light power at the distances of 0, 250, 500, 700, and 1,000 μm in the lateral direction or the vertical direction from the tip of the side-emitting optical fiber. Precisely, the number of photons, obtained from the simulation, was converted to light power [2330.5 meV/photon for 532 nm light and 2087.3 meV/photon for 594 nm light (Hesse et al., 2007)], which was adjusted to equalize the light power at 0 μm of both light wavelengths within the same model. Then, the relative input light power to deliver equal light power at each distance for both 532 and 594 nm was calculated and normalized by the input light power for 532 nm at 250 μm in the same model.

We calculated the number of photons in the lateral direction at a single depth, at the tip of the optical fiber, at a vertical depth defined as 0 mm. On the other hand, we calculated the number of photons in the vertical direction at the distances away from the tip of the side-emitting optical fiber and not from its root where the side-emission begins. As already described by Pisanello (Pisanello et al., 2017), the side-emitting optical fiber has characteristic features in its light delivery in the vertical direction that can be divided into two segments (see Figure S4). Between the root of side-emission and the tip of the optical fiber (i.e., the tapered side-emission segment), the light intensity is virtually maintained. The cortex can be illuminated efficiently in the tapered side-emission segment, and this segment covers more than 1 mm in the vertical direction in our side-emitting optical fibers (See Figure S4). Further away from the tip of the optical fiber, the scattering, as well as the absorption, affect the light propagation.

Conversion of Exp-data (firing) to Exp-data (light)

Exp-data (firing) values in Figure 4A were converted to Exp-data (light) values in Figure 4B. Exp-data (firing) reflects not only the degree of light propagation in the cortex but also the effects of wavelength-dependent

ArchT activation efficiency, while Exp-data (light) only reflects the degree of light propagation in the cortex. For conversion, we divided Exp-data (firing) values by 1.09 to obtain Exp-data (light) values. The divisor 1.09 (= 92/84) was calculated using the ArchT excitation efficiency values at 532nm (92%) and 594 nm (84%) obtained from the ArchT excitation spectrum in Figure 1A.

Estimation of the absorption coefficients for Exp-data (light)

The estimation of the absorption coefficients for the Exp-data (light) [$^{Exp}\mu_a(\lambda)$] was conducted by combining the random sampling method and evaluation of model-fitting to the experimental data. The resultant values were: $^{Exp}\mu_a(532) = 0.392$ mm^{-1}, $^{Exp}\mu_a(594) = 0.234$ mm^{-1}. Detailed procedures are described below.

For the random sampling method, we used the Monte Carlo simulations that we described above (see Transparent Method 'Monte Carlo simulation' for details). Out of the three input parameters for the Monte Carlo simulation, the scattering coefficients [$^{Exp}\mu_s(\lambda)$] and anisotropy factors [$^{Exp}\mu_{af}(\lambda)$] were assumed to be the same as in the J-model. Thus, we used the values for $^{Exp}\mu_s(\lambda)$ and $^{Exp}\mu_{af}(\lambda)$ adopted from Johansson (2010) as the fixed parameters of the simulation [$^{Exp}\mu_s(532) = {}^{J}\mu_s(532) = 10.155$ mm^{-1}, $^{Exp}\mu_s(594) = {}^{J}\mu_s(594) = 8.510$ mm^{-1}; $^{Exp}\mu_{af} = {}^{J}\mu_{af} = 0.89$ mm^{-1} for both wavelengths]. Then, absorption coefficients [$^{Exp}\mu_a(\lambda)$] were considered a free parameter of this simulation and were randomly assigned in a range from 0.1 to 0.5 mm^{-1} (Azimipour et al., 2015; Johansson, 2010; Yaroslavsky, 2002).

For evaluating the model-fitting of the simulation results to our empirical data, we first calculated the normalized input light power to deliver equal light power at the distances of 250, 500, 700, and 1,000 μm from the tip of the optical fiber in the lateral direction from the simulation results with a given absorption coefficient. We then evaluated how accurately the simulated input light power predicted the empirical input light power [Exp-data (light)] by calculating the gap between the simulated and empirical input light power with the least-squares approximation test as follows:

$$\Delta\text{InputLightPower} = \frac{\sum_{i=250,500,700,1000}[(\text{Simulated Input Light Power})_i - (\text{Empirical Input Light Power})_i]^2}{(\text{Empirical Input Light Power})_i^2}$$

To obtain a reliable ΔInputLightPower, we repeated the entire simulation (both inside- and outside-fiber simulations) 100 times and calculated the average ΔInputLightPower for each assigned value of the absorption coefficient.

We repeated the Monte Carlo simulations and least-squares approximations for different absorption coefficients until ΔInputLightPower reached the minimum plateau. Specifically, we first conducted random sampling to determine the approximate range within which the actual absorption coefficient resided. We then gradually narrowed down the range by intervals of 0.0001 mm^{-1} until we identified the minimal ΔInputLightPower. We adopted an absorption coefficient that yielded the minimal ΔInputLightPower for our [Exp-data (light)] for both 532 and 594 nm light. Note that the Exp-model is the result of applying $^{Exp}\mu_a(\lambda)$ for the simulation.

Estimation of the partial absorption coefficients of hemoglobin for Exp-data (light)

We estimated the partial absorption coefficients reflecting only the contribution of hemoglobin (Hb) [$^{Exp}\mu_{a,Hb}(\lambda)$] out of the total absorption coefficients for Exp-model [$^{Exp}\mu_a(\lambda)$] at both 532 nm and 594 nm light. Then,

we estimated the theoretical absorption coefficients for Hb in the cortex [$^{Theo}\mu_{a,Hb}(\lambda)$] with generic brain tissue modeling method (Liu et al., 2015; Mahn et al., 2018) using known extinction coefficients of oxy- and deoxy-Hb (Schmitt, 1986; Takatani and Graham, 1979). Although the contribution of oxy- or deoxy-Hb alone could not be demonstrated for $^{Exp}\mu_{a,Hb}(\lambda)$, the ratio of $^{Exp}\mu_{a,Hb}(\lambda)$ to $^{Exp}\mu_{a}(\lambda)$ and the comparison of $^{Exp}\mu_{a,Hb}(\lambda)$ to $^{Theo}\mu_{a,Hb}(\lambda)$ suggested that Hb would be mainly responsible for the observed difference between 532 and 594 nm light in our experimental data. We will describe these points in detail below.

First, to estimate $^{Exp}\mu_{a,Hb}(\lambda)$, which is the partial absorption coefficients reflecting only the contribution of Hb, we assumed that the partial absorption coefficients reflecting the contribution of the remainder of chromophore-harboring molecules other than Hb [$^{Exp}\mu_{a,other}(\lambda)$] would be the same as those of the J-model [$^{J}\mu_{a,other}(\lambda)$]. $^{J}\mu_{a,other}(\lambda)$ was estimated by subtracting $^{J}\mu_{a,Hb}(\lambda)$ from $^{J}\mu_{a}(\lambda)$, both reported in Johansson's study (Figure 6, Johansson, 2010). Accordingly, $^{Exp}\mu_{a,other}(\lambda)$ were estimated as follows: $^{Exp}\mu_{a,other}(\lambda) = {}^{J}\mu_{a,other}(\lambda) = {}^{J}\mu_{a}(\lambda) - {}^{J}\mu_{a,Hb}(\lambda)$; $^{Exp}\mu_{a,other}(532) = 0.144$ mm^{-1}, $^{Exp}\mu_{a,other}(594) = 0.075$ mm^{-1}. Then, $^{Exp}\mu_{a,Hb}(\lambda)$ was estimated by subtracting $^{Exp}\mu_{a,other}(\lambda)$ from $^{Exp}\mu_{a,}(\lambda)$ as follows: $^{Exp}\mu_{a,Hb}(\lambda) = {}^{Exp}\mu_{a}(\lambda) - {}^{Exp}\mu_{a,other}(\lambda)$; $^{Exp}\mu_{a,Hb}(532) = 0.248$ mm^{-1}, $^{Exp}\mu_{a,Hb}(594) = 0.159$ mm^{-1}.

The ratio of $^{Exp}\mu_{a,Hb}(\lambda)$ to $^{Exp}\mu_{a}(\lambda)$ [$^{Exp}\mu_{a,Hb}(532)/ {}^{Exp}\mu_{a}(532) = 0.63$, $^{Exp}\mu_{a,Hb}(594)/ {}^{Exp}\mu_{a}(594) = 0.68$] demonstrated that, among all of the chromophore-harboring molecules present, Hb is the primary component responsible for light absorption at both wavelengths of light. Moreover, the difference between 532 and 594 nm light of $^{Exp}\mu_{a,Hb}(\lambda)$ is larger than that of $^{Exp}\mu_{a,other}(\lambda)$ [$^{Exp}\mu_{a,Hb}(532) - {}^{Exp}\mu_{a,Hb}(594) = 0.089$, $^{Exp}\mu_{a,other}(532) - {}^{Exp}\mu_{a,other}(594) = 0.069$], demonstrating that Hb is the primary component responsible for the differences observed between 532 and 594 nm light in our experimental data.

Next we estimated $^{Theo}\mu_{a,Hb}(\lambda)$ with generic brain modeling method (Liu et al., 2015; Mahn et al., 2018), which uses known extinction coefficients (https://omlc.org/spectra/hemoglobin) (Schmitt, 1986; Takatani and Graham, 1979) for oxy-Hb and deoxy-Hb, the average blood volum fraction, and the Hb oxygen saturation, as follows: [$^{Theo}\mu_{a,Hb}(\lambda) = {}^{Theo}\mu_{a,oxyHb}(\lambda) + {}^{Theo}\mu_{a,deoxyHb}(\lambda)$; $^{Theo}\mu_{a,Hb}(532) = 0.398 + 0.277 = 0.675$ mm^{-1}, $^{Theo}\mu_{a,Hb}(594) = 0.126 + 0.088 = 0.214$ mm^{-1}].

Note that the above estimations of both $^{Exp}\mu_{a,Hb}(\lambda)$ and $^{Theo}\mu_{a,Hb}(\lambda)$ were based on many assumptions and approximations. For example, to estimate $^{Exp}\mu_{a,Hb}(\lambda)$ of the rat cortex, we used $^{J}\mu_{a,other}(\lambda)$ obtained from the gray matter of an adult human patient brain. To estimate $^{Theo}\mu_{a,Hb}(\lambda)$, we approximated the oxygen saturation for Hb to be 59% and the blood content to be 3.05% in the rat cortex based on previous reports (Abookasis et al., 2009; Jacques, 2013). These parameters could be affected by various factors, such as age (Jacques, 2013).

With the above assumptions/approximations, $^{Exp}\mu_{a,Hb}(\lambda)$ were smaller than $^{Theo}\mu_{a,Hb}(\lambda)$ [$^{Exp}\mu_{a,Hb}(532) < {}^{Theo}\mu_{a,Hb}(532)$, $^{Exp}\mu_{a,Hb}(594) < {}^{Theo}\mu_{a,Hb}(594)$]. Nevertheless, the relative absorption of Hb by 532 nm light to that by 594 nm light was larger than one [$^{Exp}\mu_{a,Hb}(532)/{}^{Exp}\mu_{a,Hb}(594) = 1.56$, $^{Theo}\mu_{a,Hb}(532)/ {}^{Theo}\mu_{a,Hb}(594) = 3.15$] for both $^{Exp}\mu_{a,Hb}(\lambda)$ and $^{Theo}\mu_{a,Hb}(\lambda)$. That is, $^{Exp}\mu_{a,Hb}(\lambda)$ showed the same qualitative wavelength-dependent change as $^{Theo}\mu_{a,Hb}(\lambda)$ between 532 nm and 594 nm.

Statistical analysis

To compare the light emission area in the fluorescence images between the blunt-end and side-

emitting optical fiber types (n = 6, for each) (Figure 1B), the maximum pixel value was normalized to 100 for each fiber. We then plotted the peak normalized illuminance against distance from the tip of optical fiber separately for the lateral and axial directions. We compared the illuminance between the two fiber types in each bin (at the equal distance from the fiber tip) by using a two-sample unpaired t test with Bonferroni correction (219 bins for the lateral direction and 382 bins for the axial direction). To evaluate the differences in power-suppression curves between 532 nm light and 594 nm light (Figure 2D and 2E), we compared the slopes for EP50 (Figure 2F) by using the two-tailed unpaired t test. The mean supEff values at the upper limit of the dynamic range (Figure 2G) were compared by using the two-tailed paired multiple t tests with Bonferroni corrections. For the comparisons of supEff between the two wavelengths of light with the same input light power at each distance, we used two-way repeated measures analysis of variance (ANOVA) followed by Bonferroni's multiple comparisons (Figure 3C, S2A, S3F). For the evaluations of the effects of distance on the relative supEff (532 nm / 594 nm), we applied the one-way repeated measures ANOVA with the main effect of the four distances (Figure 3D, S2B, S3G) followed by Tukey-Kramer multiple comparisons. To compare the peak-valley height of spikes, we used two-way repeated measures ANOVA (Figure S3B). To estimate the light power required for equivalent neural suppression with 594 nm light versus 532 nm light (Figure 4A), we included 9 units in our analyses for which we obtained supEff in all four distance conditions. To evaluate the effect of distance and wavelengths for the estEP50, we applied two-way repeated-measures ANOVA with the main effect of two wavelengths of the light and the four distances (Figure 4A). All statistical tests were performed using GraphPad Prism software (GraphPad Software, La Jolla, CA, USA). Each plot with an error bar in each figure indicates the mean and standard error, but only in Figure 1B, the error bar indicates standard deviation.

Supplementary Reference:

Abookasis, D., Lay, C.C., Mathews, M.S., Linskey, M.E., Frostig, R.D., and Tromberg, B.J. (2009). Imaging cortical absorption, scattering, and hemodynamic response during ischemic stroke using spatially modulated near-infrared illumination. J Biomed Opt *14*, 024033.

Azimipour, M., Atry, F., and Pashaie, R. (2015). Effect of blood vessels on light distribution in optogenetic stimulation of cortex. Opt Lett *40*, 2173-2176.

Hesse, M., Meier, H., and Zeeh, B. (2007). Spectroscopic Methods in Organic Chemistry, 2nd edn (Georg Thieme Verlag).

Jacques, S.L. (2013). Optical properties of biological tissues: a review. Physics in medicine and biology *58*, R37-61.

Johansson, J.D. (2010). Spectroscopic method for determination of the absorption coefficient in brain tissue. J Biomed Opt *15*, 057005.

Liu, Y., Jacques, S.L., Azimipour, M., Rogers, J.D., Pashaie, R., and Eliceiri, K.W. (2015). OptogenSIM: a 3D Monte Carlo simulation platform for light delivery design in optogenetics. Biomed Opt Express *6*, 4859-4870.

Mahn, M., Gibor, L., Patil, P., Cohen-Kashi Malina, K., Oring, S., Printz, Y., Levy, R., Lampl, I., and Yizhar, O. (2018). High-efficiency optogenetic silencing with soma-targeted anion-conducting channelrhodopsins. Nature communications *9*, 4125.

Matsuyama, M., Ohashi, Y., Tsubota, T., Yaguchi, M., Kato, S., Kobayashi, K., and Miyashita, Y. (2015). Avian sarcoma leukosis virus receptor-envelope system for simultaneous dissection of multiple neural circuits in mammalian brain. Proc Natl Acad Sci U S A *112*, E2947-2956.

Mattis, J., Tye, K.M., Ferenczi, E.A., Ramakrishnan, C., O'Shea, D.J., Prakash, R., Gunaydin, L.A., Hyun, M., Fenno, L.E., Gradinaru, V.*, et al.* (2011). Principles for applying optogenetic tools derived from direct comparative analysis of microbial opsins. Nature methods *9*, 159-172.

Owen, S.F., Liu, M.H., and Kreitzer, A.C. (2019). Thermal constraints on in vivo optogenetic manipulations. Nat Neurosci *22*, 1061-1065.

Pisanello, F., Mandelbaum, G., Pisanello, M., Oldenburg, I.A., Sileo, L., Markowitz, J.E., Peterson, R.E., Della Patria, A., Haynes, T.M., Emara, M.S.*, et al.* (2017). Dynamic illumination of spatially restricted or large brain volumes via a single tapered optical fiber. Nat Neurosci *20*, 1180-1188.

Schmitt, J.M. (1986). Optical Measurement of Blood Oxygen by Implantable Telemetry (Stanford University).

Setsuie, R., Wang, Y.L., Mochizuki, H., Osaka, H., Hayakawa, H., Ichihara, N., Li, H., Furuta, A., Sano, Y., Sun, Y.J.*, et al.* (2007). Dopaminergic neuronal loss in transgenic mice expressing the Parkinson's disease-associated UCH-L1 I93M mutant. Neurochem Int *50*, 119-129.

Sileo, L., Bitzenhofer, S.H., Spagnolo, B., Pöpplau, J.A., Holzhammer, T., Pisanello, M., Pisano, F., Bellistri, E., Maglie, E., De Vittorio, M.*, et al.* (2018). Tapered Fibers Combined With a Multi-Electrode Array for Optogenetics in Mouse Medial Prefrontal Cortex. Frontiers in neuroscience *12*.

Stujenske, J.M., Spellman, T., and Gordon, J.A. (2015). Modeling the Spatiotemporal Dynamics of Light and Heat Propagation for In Vivo Optogenetics. Cell reports *12*, 525-534.

Takatani, S., and Graham, M.D. (1979). Theoretical analysis of diffuse reflectance from a two-layer tissue model. IEEE transactions on bio-medical engineering *26*, 656-664.

Tamura, K., Ohashi, Y., Tsubota, T., Takeuchi, D., Hirabayashi, T., Yaguchi, M., Matsuyama, M., Sekine, T., and Miyashita, Y. (2012). A glass-coated tungsten microelectrode enclosing optical fibers for optogenetic exploration in primate deep brain structures. J Neurosci Methods *211*, 49-57.

Tamura, K., Takeda, M., Setsuie, R., Tsubota, T., Hirabayashi, T., Miyamoto, K., and Miyashita, Y. (2017). Conversion of object identity to object-general semantic value in the primate temporal cortex. Science *357*, 687-692.

Tsubota, T., Okubo-Suzuki, R., Ohashi, Y., Tamura, K., Ogata, K., Yaguchi, M., Matsuyama, M., Inokuchi, K., and Miyashita, Y. (2015). Cofilin1 controls transcolumnar plasticity in dendritic spines in adult barrel cortex. PLoS Biol *13*, e1002070.

Yaroslavsky, A.N. (2002). Optical properties of selected native and coagulated human brain tissues in vitro in the visible and near infrared spectral range. Phys Med Biol *47*, 2059-2073.